J Reiser et al.

Ductilisation of tungsten (W): On the shift of the brittle-to-ductile transition (BDT) to lower temperatures through cold-rolling

Preprint of Paper to be submitted for publication in International Journal of Refractory Metals and Hard Materials

Ductilisation of tungsten (W): On the shift of the brittle-to-ductile transition (BDT) to lower temperatures through cold-rolling

Jens Reiser[a,], Jan Hoffmann[a], Ute Jäntsch[a], Michael Klimenkov[a], Simon Bonk[a], Carsten Bonnekoh[a], Michael Rieth[a], Andreas Hoffmann[b], Tobias Mrotzek[b]*

a: Karlsruhe Institute of Technology, Institute for Applied Materials, 76344 Eggenstein-Leopoldshafen, Germany
b: PLANSEE SE, 6600 Reutte, Austria

Corresponding author:
*:   Dr. Jens Reiser, Karlsruhe Institute of Technology (KIT), Institute for Applied Materials (IAM-AWP), Hermann-von-Helmholtz-Platz 1, 76344 Eggenstein-Leopoldshafen, Germany, Phone: +49 721 608 23894, E-Mail: jens.reiser@kit.edu

Highlights:

- The BDT temperature correlates with the grain size
- The BDT temperature obeys an equation of the Hall-Petch form
- The smaller the grain size, the lower the BDT temperature
- The shift of the BDT temperature relates to the availability of dislocation sources

Keywords:

- polycrystalline tungsten (W)
- brittle-to-ductile transition (BDT)
- grain size
- Hall-Petch relation
- dislocations

Abstract

Here we show that cold-rolling decreased the brittle-to-ductile transitions (BDT) temperature of tungsten (W). Furthermore, we show that the BDT temperature correlates with the grain size (the smaller the grain size, the lower the BDT temperature) following a Hall-Petch-like equation. This relation between the grain size and the BDT temperature is well known from ferrous materials and is generally accepted in the steel community.

Our ductilisation approach is the modification of the microstructure through cold-rolling. In this work we assess three different microstructures obtained from (i) hot-rolled, (ii) cold-rolled, and (iii) hot-rolled and annealed (1 h / 2000°C, annealed in H_2) tungsten plates. From these plates Charpy impact test samples with dimensions of 1 x 3 x 27 mm^3, without notch, were cut and tested in the L-S and T-S directions. The results show the following BDT temperatures: 675°C / 948 K (L-S, "annealed"), 375°C / 648 K (L-S, "hot-rolled") and 125°C / 398 K (L-S, "cold-rolled"). The microstructure of the plates is analysed by means of SEM (EBSD: grain size, subgrains, texture, KAM), FIB (channelling contrast) and TEM analyses (bright field imaging).

The question of how cold-rolling decreases the BDT temperature is discussed against the background of (i) microcracking, crack branching, and crack bridging effects, (ii) texture effects, (iii) the role of dislocations and (iv) the impact of impurities, micropores, and sinter pores. Our results suggest that the availability of dislocation sources (dislocation boundaries, grain boundaries; in particular IDBs and HAGBs) is the most important parameter responsible for the increase of the cleavage resistance stress, σ_F, or the decrease of the BDT temperature respectively.

1. Introduction

Certain features of the low temperature deformation behaviour of metals and alloys with body-centred cubic (bcc) structure distinguish the whole group from face-centred cubic (fcc) and hexagonal close-packed (hcp) metals and alloys. These features include (i) the striking violation of Schmid's law (anomalous slip) [1,2], (ii) the existence of a knee temperature, T_K, (formerly called the critical temperature; approx. 0.2 * T_m, T_m melting temperature) [3,4], (iii) the rapid increase of the flow stress with decreasing temperature (for $T < T_K$), (iv) the strain-rate dependence of the flow stress (for $0\ K < T < T_K$), and (v) the brittle-to-ductile transition (BDT) [4,5].

In view of the important economic role of metals and alloys with bcc structure, understanding the origin of these phenomena is of the utmost importance. Here, the description of the structure and properties of screw dislocations (non-planar core structure) [6,7] as well as the description of the mobility of the ½ <111> screw dislocations (nucleation of pairs of kinks) [8] has proved extremely successful.
Nevertheless, an in-depth understanding of the controlling mechanisms of the BDT is still lacking. In particular, the BDT of textured and pre-deformed bcc materials is still less well understood and the role of dislocations, microcracking, branching of the main crack, and crack bridging effects has not been elucidated yet [9].
In this paper we present and discuss the results of a study on the BDT of textured and pre-deformed tungsten (W) plates. In particular, we address the question whether cold-rolling, hot-rolling, and annealing have an impact on the BDT of tungsten plates. The following chapters will provide answers to the following questions:

(1) How does the BDT temperature change with cold-rolling?
(2) Can a correlation between microstructural features (hardness, grain size, dislocation density) and the BDT temperature show some trends?
(3) What is the role of dislocations and other toughening mechanisms (microcracking, branching of the main crack and crack bridging effects) on the shift of the BDT?

The paper is organized as follows: a short literature review of the research on the BDT is given in the following section. Afterwards, the fabrication of the tungsten plates is described, followed by the presentation of the results of the Charpy impact tests. Finally, the microstructure of the tungsten plates is analysed and a correlation between microstructure and BDT is discussed.

2. Background: the brittle-to-ductile transition (BDT)

For the BDT, the shielding and blunting (anti-shielding) of a crack tip plays an important role. It is realized by the emission of dislocations, which is a two-step process starting with (i) the nucleation of dislocations followed by (ii) the dislocations glide (Figure 1). Models describing the BDT as a nucleation-controlled event assume that the lack of active dislocation sources prevents the emission of a sufficient number of dislocations to provide an effective shielding

[10,11]. Models describing the BDT as a mobility-controlled event assume that dislocations are generated in large numbers but cannot leave the crack tip region fast enough, and thus inhibit the instantaneous nucleation of further dislocations [12,13].

Despite great efforts, the question whether the BDT is controlled by dislocations nucleation or dislocation mobility is still unanswered. In other words, the understanding of the mechanisms limiting the plastic deformation of the crack tip region is still unclear.
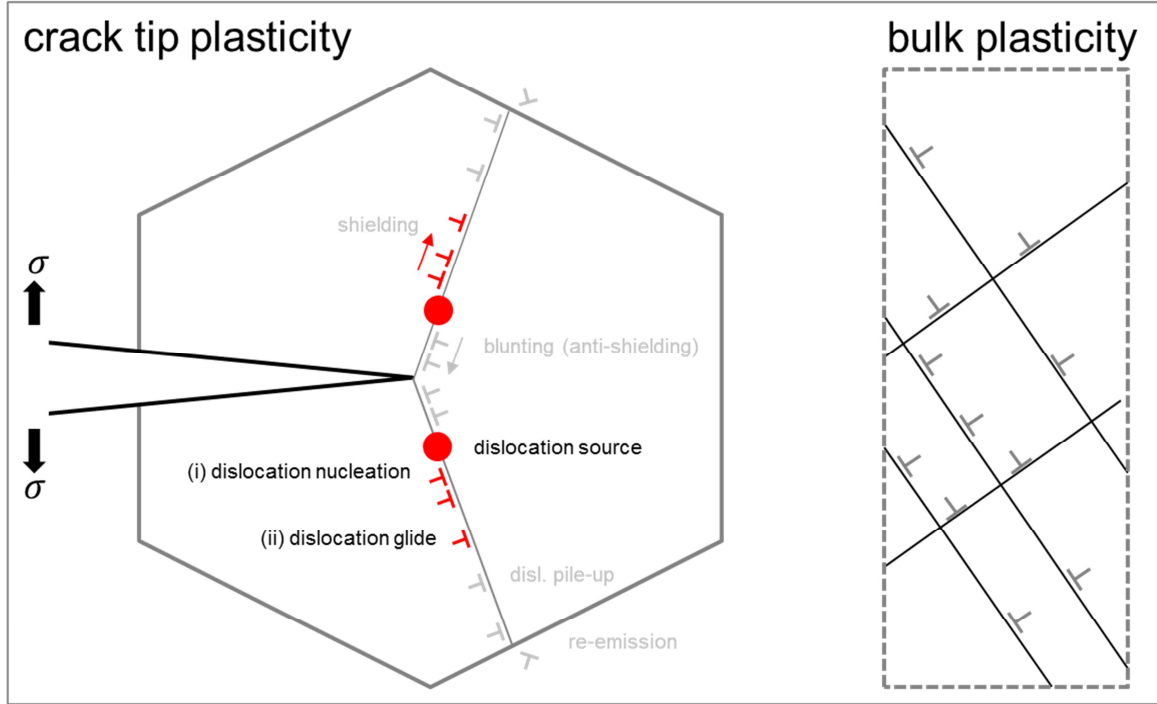
Figure 1. Schematic differentiation between (i) dislocation nucleation and (ii) dislocation glide at the crack tip. The drawing on the left represents crack tip plasticity, the drawing on the right displays bulk plasticity. The symbol for edge dislocations was used to represent dislocation glide of any kind, e.g. screw and non-screw dislocation motion.

The investigations to identify the controlling mechanisms of the BDT have been done using both an indirect (determination and comparison of activation energies or activation enthalpies [9,14,15,16]) and a direct approach (in situ transmission electron microscopy (TEM) [17,18,19]).

The indirect approaches make use of the fact that the relationship between the applied strain rate, $\dot{\varepsilon}$, and the BDT temperature, T_{BDT}, is given by

$$\dot{\varepsilon} = A \cdot \exp\left(-\frac{Q_{BDT}}{k_B \cdot T_{BDT}}\right), \tag{1}$$

with k_B being the Boltzmann's constant, Q_{BDT} the activation energy for the BDT, and A is a constant [20]. This empirically derived activation energy can now be compared with thermodynamically well-defined activation energies and activation enthalpies.

The activation energy for dislocation motion, Q_{dis}, can be derived from the simplest and most approximate description of the mobility of the dislocations:

$$V_d(\tau, T) = V_0 \left(\frac{\tau}{\tau_0}\right)^{m(T)} \exp\left(-\frac{Q_{dis}}{k_B \cdot T}\right), \tag{2}$$

where the dislocations velocity, $V_d(\tau, T)$, depends on the resolved shear stress, τ, the stress exponent, m, the temperature, T, and the activation energy for dislocation motion, Q_{dis}. V_0 is a pre-exponential factor with the units of a velocity, and τ_0 = 1 MPa simply fixes the units of the stress [9].

For various materials such as silicon (Si) [12], germanium (Ge) [16], and alumina (Al_2O_3) [16] the activation energy for the BDT, Q_{BDT}, was found to be equal to the activation energy for dislocation motion, Q_{dis}. Thus the process controlling the BDT is proposed to be dislocation glide in the region near the crack tip, rather than dislocation nucleation at or near the crack tip [12].

While this approach worked well for various semiconductors, it cannot be applied to tungsten due to the lack of experimental data regarding the dislocations velocity, $V_d(\tau, T)$, and consequently the activation energy for dislocation motion, Q_{dis} [15]. The only study on dislocation velocity in tungsten gave data for non-screw dislocations ($Q_{dis}^{non-screw} = 0.2 - 0.5$ eV) [21], while the activation energy needed for the glide of screw dislocations in tungsten (or more precisely for the formation of a kink-pair on a screw dislocation), Q_{dis}^{screw}, is estimated to be > 1 eV [16].

Assuming that the BDT in tungsten is controlled by dislocation velocity, then the likely controlling factor is the mobility of the screw dislocations, since their mobility is slow compared to that of non-screw dislocations [16]. It is popularly believed that screw dislocation motion proceeds via the nucleation of kink-pairs (steps on the dislocation line) and their subsequent lateral relaxation [22]. According to Seeger's theory of kink-pair formation [22], an effective kink-pair formation enthalpy, $H_{kp}(\sigma^*)$, which can be identified as the activation enthalpy for screw dislocation motion, can be written as

$$H_{kp}(\sigma^*) = 2H_k - 2\alpha\sqrt{\sigma^*} \text{ , with } \alpha = \left(\frac{a^3 b \gamma_0}{2}\right)^{1/2} \quad (3)$$

where σ^* is the resolved shear stress, $2H_k$ is the enthalpy for kink-pair formation, a is the distance between two adjacent Peierls valleys connected by a kink in a dislocation with Burgers vector b, and γ_0 is a pre-factor of the logarithmic expression of the dislocation line tension [23].

Giannattasio and Roberts investigated the BDT of tungsten single-crystals with a crack system of {100}<001> (i.e. {100} crack plane and <001> crack front) [15]. They determined an activation energy for the BDT, Q_{BDT}, of 1.00 ± 0.04 eV. Next, the authors calculated the effective kink-pair formation enthalpy, $H_{kp}(\sigma^*)$, to be 1.11 eV. As both values are very close, the authors propose that for {100} cracks in tungsten, the BDT is controlled by the motion of screw dislocations [16].

Gumbsch et al. reported experiments on the BDT of tungsten single-crystals with a crack system of {110}<1$\overline{1}$0> [14]. They deduced an activation energy for the BDT, Q_{BDT}, of approximately 0.2 eV. This activation energy is close to the activation energy for the glide of non-screw dislocations ($Q_{dis}^{non-screw} = 0.2 - 0.5$ eV). As bulk plasticity is believed to be controlled by the mobility of screw dislocations which require an activation energy > 1eV, the authors conclude that crack tip plasticity cannot be limited by the same mechanisms as bulk plasticity.

Furthermore, Giannattasio, Roberts et al. investigated the BDT temperature of notched and un-notched bars made of polycrystalline tungsten [24]. The activation energy for the BDT, Q_{BDT}, was equal to 1.0 eV in both the notched and un-notched specimens. According to the authors, this result indicates that the activation energy for the BDT, Q_{BDT}, is a materials parameter, independent of geometrical factors.

Rupp and Weygand studied the BDT of sintered and rolled tungsten rods. The rods experienced a degree of deformation of 65 % [25]. For samples with C-R orientation an

activation energy for the BDT, Q_{BDT}, of 1.44 eV, and for the R-L orientation an activation energy for the BDT, Q_{BDT}, of 1.32 eV was determined [26]. The conclusion from Rupp is in line with the argumentation from Roberts: the BDT is controlled by the glide of screw dislocations, or more precisely, by the nucleation of kink-pairs.

Zeng and Hartmaier [27] studied the fracture toughness of polycrystalline tungsten as a function of grain size. Their numerical results reveal that grain boundaries may confine the plastic zone (for small grain sizes and low loading rates, dislocations reach the grain boundaries). Thus, the shielding dislocations pile-up at the grain boundary closest to the crack-tip, which causes high stresses in the neighbouring grain. This in turn can trigger the plastic yielding of that grain. Hartmaier [28] brought forward the hypothesis that the activation energy for the BDT in a polycrystal should be related to the dislocation-grain-boundary-interaction energy (dislocation absorption/renucleation, activation of slip systems in the neighbouring grain).

Németh et al. evaluated the nature of the BDT of annealed coarse-grained and as-received ultrafine-grained (UFG) tungsten foil [29]. The activation energy for the BDT, Q_{BDT}, for the coarse-grained material was found to be 2.9 (+2.6/−0.9) eV. On account of this energy, the authors conclude that screw dislocation motion controls the BDT in the annealed tungsten foil. For the UFG tungsten foil they determined a BDT temperature of about 77 K. The authors assume that the thermal activation of screw dislocation motion is impossible at such low temperatures and that thus the BDT in UFG tungsten is controlled by the glide of non-screw dislocations. The work of Németh et al. leaves the question open whether the BDT temperature decreases continuously through cold-rolling, or if a decrease of the BDT temperature requires a UFG microstructure. The answer to this question will be given in this paper.

A summary of the investigated BDTs in tungsten can be found in Table 1.

Table 1: Summary of the activation energy for the BDT, $\mathbf{Q_{BDT}}$, obtained from tungsten single crystals and polycrystalline tungsten material. The interpretation of the activation energy for the BDT, $\mathbf{Q_{BDT}}$, is shown in the right-hand column.

Authors	W material	Result: Q_{BDT}; T_{BDT}	BDT controlled by / comment
Giannattasio and Roberts [16]	single crystal, {100}<001>	1.00 ± 0.04 eV	"Glide of screw dislocations"
Gumbsch et al. [14]	single crystal, {110}<1$\bar{1}$0>	0.2 eV	"Crack tip plasticity cannot be limited by the same mechanisms as bulk plasticity"
Giannattasio, Roberts et al. [24]	notched and un-notched polycrystalline W	1.00 eV	"Q_{BDT} is a materials parameter, independent of geometrical factors"
Rupp and Weygand [25,26]	polycrystalline rods	1.44 eV (C-R), 1.32 eV (R-L)	"Glide of screw dislocations"
Németh et al. [29]	coarse-grained foil	2.9 (+2.6/−0.9) eV	"Glide of screw dislocations"
Hartmaier [28]	fine-grained	grain boundaries confine the plastic zone	"Q_{BDT} should be related to the dislocation-grain-boundary-interaction energy (dislocation absorption/renucleation, activation of slip systems in the neighbouring grain)"
Németh et al. [29]	ultrafine-grained foil	77 K	"Glide of non-screw dislocations"

3. Materials and methods

This chapter is divided into three parts. In the first part we provide a detailed description of the fabrication history of the plates, including details on the rolling process, the rolling temperature and the rolling reduction. After that, the experimental set-up for the Charpy impact tests is presented and finally information about the electron microscopy analyses is displayed.

3.1. Materials and test samples

The tungsten materials assessed in this work are technically pure tungsten plates (> 99.97 wt % W) manufactured by PLANSEE SE in a powder metallurgical route consisting of sintering and rolling. The impurity concentrations which PLANSEE SE guarantees not to exceed, as well as the typical impurity concentrations, are shown in Table 2 [30].

Table 2: Impurity concentration of the tungsten plates. The first line shows the maximum concentration of selected elements which PLANSEE SE guarantees not to exceed, while the second line gives the average impurity concentrations.

Element	C	H	N	O	P	S	Si
Guaranteed analyses (max.), $\mu g/g$	30	5	5	20	20	5	20
Typical analyses (max.), $\mu g/g$	10	2	<2	5	<10	<2	5

In this work, we assess three different microstructures obtained from (i) hot-rolled, (ii) cold-rolled, and (iii) hot-rolled and annealed (1 h / 2000°C, annealed in H_2) tungsten plates.

The fabrication route of the materials "Mat1-rxx", and "Mat1" was as follows: A sinter ingot (No. 1) with a height of h_0 was reduced to a height of h_1 by hot-rolling. We define hot-rolling as rolling above the recrystallization temperature of tungsten, thus rolling above 1200°C. Consequently, we define cold-rolling as rolling below 1200°C. The final thickness of the plate was greater than 1 mm. The plate was cut into two pieces. The first part was stress-relieved. This plate is referred to as "hot-rolled" ("Mat1") within this paper. The second part was annealed for 1 h at 2000°C in hydrogen. This plate is referred to as "annealed" ("Mat1-rxx") in this paper.

The fabrication route of the material "Mat2" was as follows: A sinter ingot (No. 2) with a height of h_0 was reduced to a height of h_1 by hot-rolling. After that the plate was cold-rolled to a final thickness h_2. The plate experienced a reduction of the thickness through cold-rolling of ln (h_1/h_2) = 0.69 and the final thickness of the plate was greater than 1 mm. After cold-rolling the plate was stress-relieved. This plate is referred to as "cold-rolled" ("Mat2") within this paper.

For each material the rolling direction was unidirectional; there was no change of the rolling direction. A summary of the fabrication history of each plate can be found in Table 3. Due to the high degree of hot- and cold-rolling, we assume the density to be close to the theoretical density for all the plates.

Table 3: Material nomenclature, material processing history and the degree of cold-rolling experienced by the three types of materials assessed within this study.

	Mat1-rxx	Mat1	Mat2
Referred to as:	"annealed"	"hot-rolled"	"cold-rolled"

Sinter ingot	number	# 1	# 1	# 2
	chemical composition	> 99.97 wt % W	> 99.97 wt % W	> 99.97 wt % W
	height	h_0	h_0	h_0
Processing	step 1: hot-rolling (> 1200°C)	from h_0 to h_1	from h_0 to h_1	from h_0 to h_1
	step 2: annealing in H_2	1 h / 2000°C	-	-
	step 3: cold-rolling (< 1200°C)	-	-	from h_1 to h_2
	step 4: stress relieving	-	X	X
	rolling direction	unidirectional	unidirectional	unidirectional
Degree of cold-rolling, ln (h_x / h_{x+1})		-	0	0.69
Final thickness of the plate		> 1 mm	> 1 mm	> 1 mm

From these plates, Charpy impact test samples with dimensions of 1 x 3 x 27 mm^3, without notch, were cut and tested in the L-S and T-S directions.

3.2. Charpy impact tests

Instrumented Charpy impact tests were performed according to the DIN EN ISO 148-1 (2011) and DIN EN ISO 14556 (2006) standards. These standards describe small size specimens with dimensions of 27 mm x 3 mm x 4 mm, 1 mm notch depth, 0.1 mm notch root radius, and a support span of 22 mm (KLST type sample). In this study we changed the dimensions of the samples to 27 mm x 3 mm x 1 mm, without notch.
The samples were cut from the "annealed", "hot-rolled" and "cold-rolled" materials in the L-S and T-S orientations (details on the two-letter code can be found in Ref. [31]). The cutting method was spark erosion. One side of the sample contained the original rolled surface; the other side contained the eroded surface. The samples were positioned in such a way that the striker hit the eroded surface first. More details on the sample preparation, including the surface roughness of each material, can be found in Table 4.

Table 4: Charpy impact test sample preparation and sample orientation.

|		Mat1-rxx	Mat1	Mat2
Referred to as:		"annealed"	"hot-rolled"	"cold-rolled"
Dimensions [mm]		1 x 3 x 27, w/o notch	1 x 3 x 27, w/o notch	1 x 3 x 27, w/o notch
Sample orientations		L-S, T-S	L-S, T-S	L-S, T-S
Contour cut by spark erosion		X	X	X
Surface # 1: cut by spark erosion		X	X	X
Surface # 2: as-delivered		X	X	X
Striker hit the spark eroded surface: → crack start at surface # 2		X	X	X
Roughness, R_a, of surface # 2 [μm]	in L-direction	1.7 ± 0.33	1.36 ± 0.31	1.5 ± 0.1
	in T-direction	2.16 ± 0.27	1.37 ± 0.35	1.6 ± 0.03

The striker has a radius of 2 mm and a rated initial potential energy of 22.6 J. The impact speed is 3.85 m/s. For a sample representing the upper shelf energy (USE) (e.g. "cold-rolled", L-S, 150°C), the duration of a test is about 2500 μs, with a maximum force of about 1560 N. Making use of the Euler–Bernoulli beam theory, the maximum tensile stress, σ_b^{max}, experienced by the sample can be expressed as

$$\sigma_b^{max} = \frac{M_{by}}{I_y} * z \tag{4}$$

where M_{by} is the bending moment, I_y is the second moment of area, and z is the distance from the neutral axis to the surface of the sample. Based on this stress calculation, an outer fibre strain rate, $\dot{\varepsilon}$, of 267.9 1/s can be deduced.

The Charpy impact test device is designed in a drop-weight style (Figure 2). To avoid oxidation, the whole Charpy testing machine is placed inside a vacuum vessel which operates at typical pressures of about 1 x 10^{-3} mbar. The specimens are heated up together with the support, which allows precise test temperature control. For more technical details of the Charpy impact test device, the reader is referred to Ref. [32].

The Charpy impact test results display the dissipated energy plotted against the test temperature. In this study, at least one sample for each material condition and test temperature was tested. In order to verify the reproducibility of the results, the BDT temperatures were confirmed by further selected tests (further experiments of the highest temperature of the lower shelf energy (LSE) and of the lowest temperature of the USE).
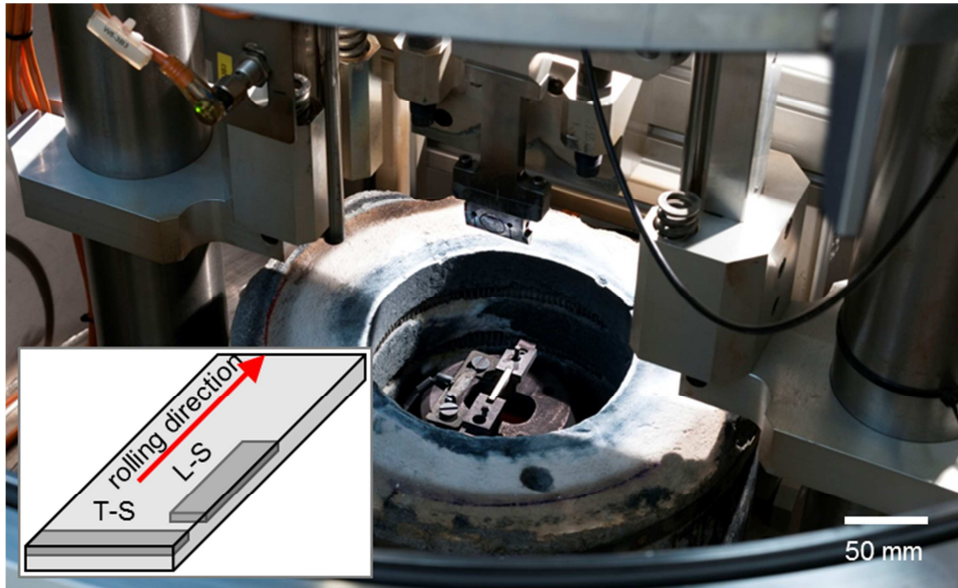
Figure 2. Charpy impact test device, designed in a drop weight style.

The value of the BDT temperature was determined from the Charpy curve as the temperature corresponding to half the value of the upper shelf energy.

3.3. EBSD measurements

Electron backscatter diffraction (EBSD) measurements were performed using a Zeiss Merlin scanning electron microscope (SEM) equipped with an EDAX Hikari camera. The experiments were done using an acceleration voltage of 20 kV and 10 nA probe current. For the mappings in Figure 10 and Figure 17, areas of 140 µm by 140 µm with a step size of 200 nm (or 400 nm for the "annealed" material) were chosen, whereas for the mappings in Figure 12, areas of 40 µm by 30 µm with a step size of 30 nm (or 400 nm for the "annealed" material) were chosen.

Points with a confidence index (CI) lower than 0.1 were removed during post-processing. Apart from a grain CI standardization, no cleanup of the datasets was performed. The orientations of the data points remained unchanged. Misorientations between 5° and 15°

were considered as low angle grain boundaries (LAGBs, or subgrain boundaries, highlighted in white in the inverse pole figure (IPF) map or in red in the grain boundary map respectively), while misorientations exceeding 15° were considered as high angle grain boundaries (HAGBs, highlighted in black). Kernel average misorientation (KAM) maps were calculated using only 1st neighbour points with misorientations between 0° and 5°. IPF maps are displayed with respect to the orthogonal sample directions.

The grain sizes were calculated using the EBSD data. The grain boundary intercepts (only HAGBs were considered) of at least 130 lines running in the L-, T-, or S-directions were calculated using the EDAX OIM data analysis software. The average intercept length over all lines of each direction is given in Figure 11.

The textures were calculated from the EBSD data using a harmonic series expansion following the formulation of Bunge. The degree used for the calculation is 15, and the Euler angles are noted in the Bunge convention. The main texture components are displayed in the $\varphi_2 = 45°$-sections of the orientation distribution function (ODF) maps.

3.4. TEM analyses

The tungsten specimens for TEM investigation were prepared by Focused Ion Beam (FIB) methods using an AURIGA CrossBeam system from Carl Zeiss. The lamellas of 200 – 300 nm thickness were additionally flash polished [33] at 12 V for 50 ms to remove thin layer which was damaged during FIB preparation.

The TEM investigations were performed using a Tecnai 20 FEG transmission electron microscope from FEI. The microscope has an accelerating voltage of 200 kV and a 0.14 nm resolution limit. The tungsten structure was imaged by using conventional bright field microscopy with an ORIUS SC600 pre-column camera.

4. Results

This chapter is organized as follows. The results of the Charpy impact tests are displayed, including an analysis of the fractured surfaces. This is followed by in-depth microstructural analyses addressing issues like hardness (HV0.1), surface quality, grain size (EBSD), crystallographic texture (EBSD), and dislocation distribution (TEM).

4.1. Results of the Charpy impact tests

The results of the Charpy impact test are displayed in Figure 3, where the dissipated energy is plotted against the test temperature. All material classes ("hot-rolled", "cold-rolled", and "annealed") show a clear transition from brittle fracture (at lower temperatures) to ductile (at higher temperatures). Images of selected samples showing the brittle-to-ductile transition can be found in Figure 4. These images show that the samples of the brittle regime are broken into two pieces, whereas all the samples of the ductile regime are fully ductile and do not show any stopped cracks.
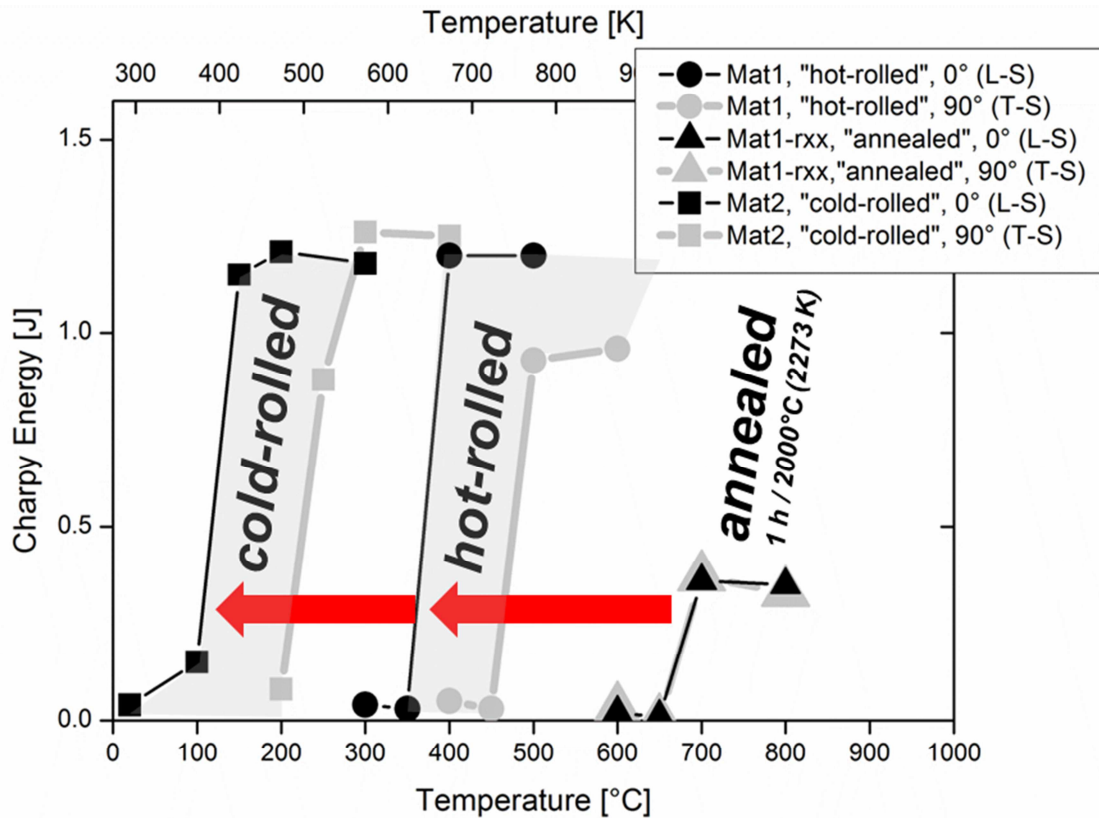
Figure 3. Results of the Charpy impact tests.

The USE for the "hot-rolled" and "cold-rolled" materials is about 1.2 J and for the "annealed" material the USE is about 0.4 J. It will be shown later that the USE correlates with the hardness (HV0.1).
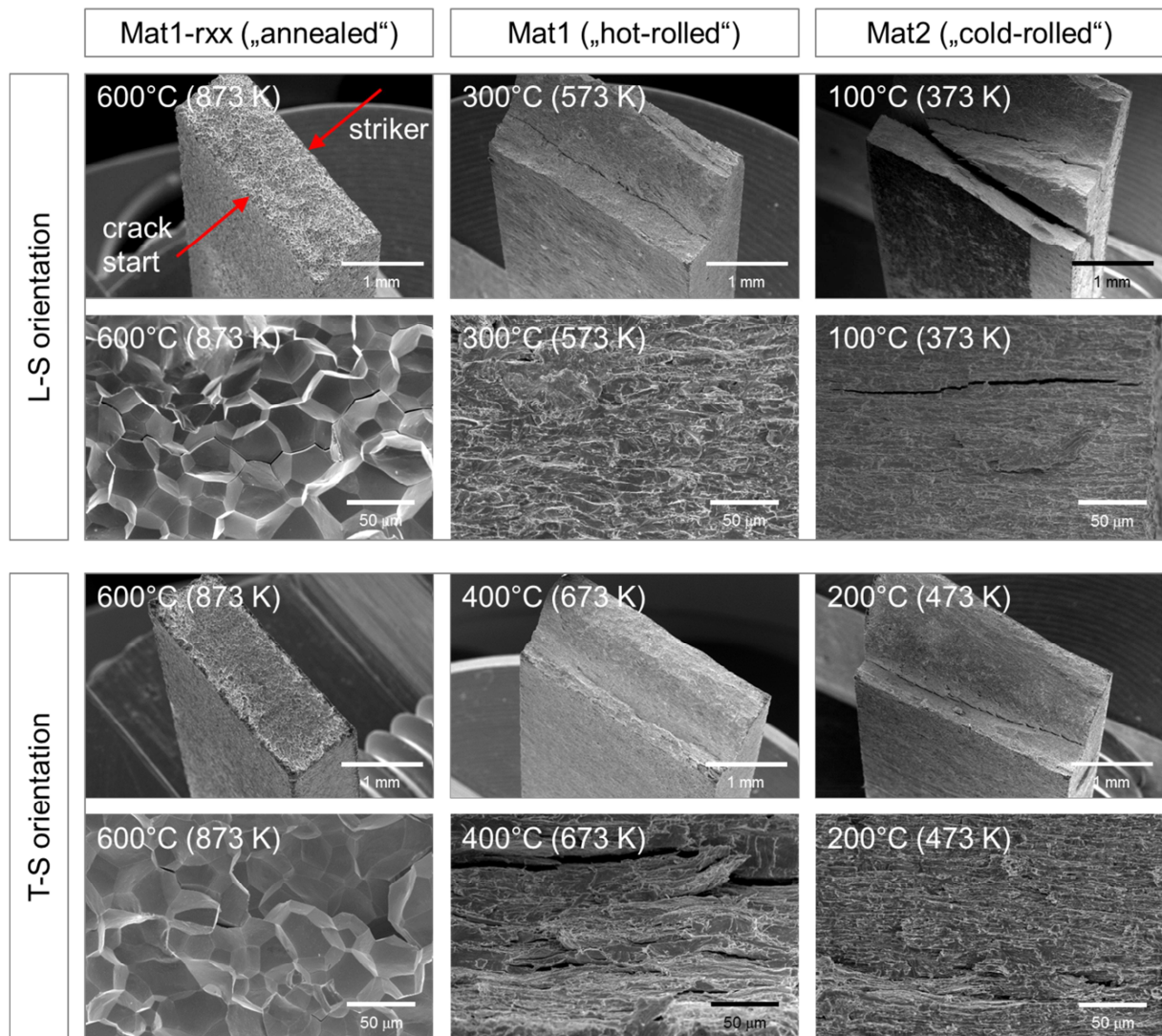
The BDT temperature for the "annealed" material is equal in both the L-S and T-S directions and is at 675°C (948 K). For the "hot-rolled" and "cold-rolled" material the BDT temperature decreases significantly ("hot-rolled", L-S: 375°C / 648 K; "cold-rolled", L-S: 125°C / 398 K). This decrease is accompanied by the formation of an anisotropic material response, as the L-S and T-S oriented samples behave differently. There is a common trend that the BDT temperature of the samples tested in L-S is about 100 K lower than that of samples tested in the T-S direction.
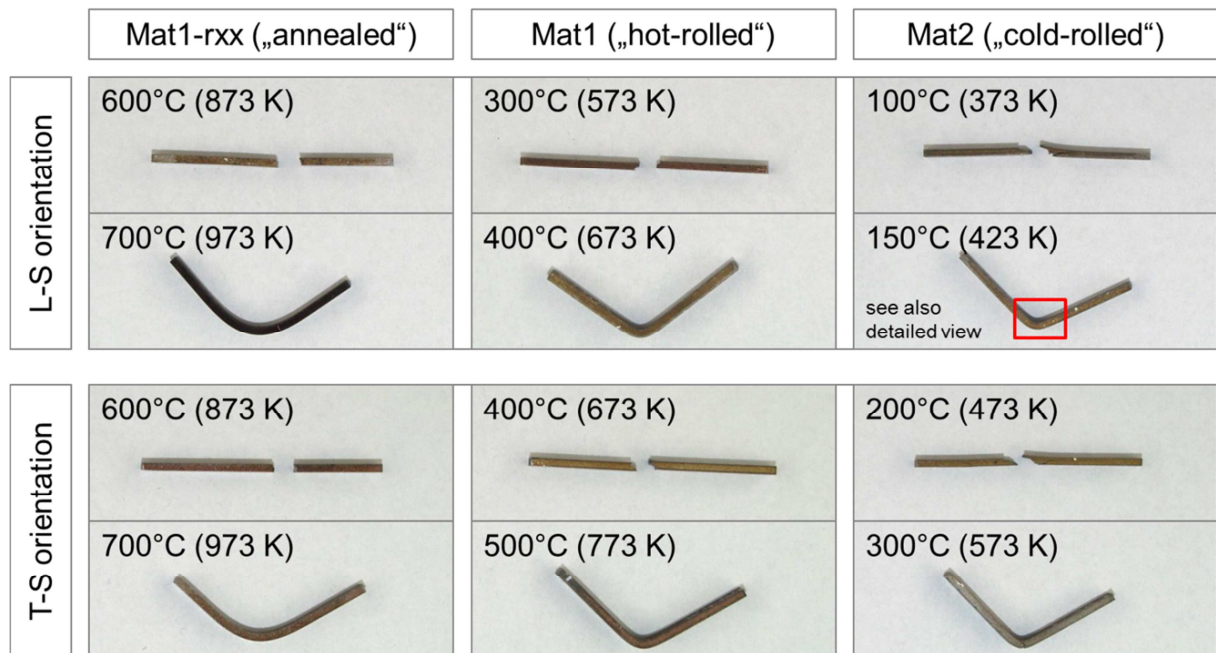
Figure 4. Images of selected samples showing the brittle-to-ductile transition. A detailed analysis of the deformed microstructure of the tested sample, "cold-rolled", L-S, tested at 150°C, can be found in the Discussion section.

The analyses of the fractured surfaces (samples of the brittle regime) show same essential features (Figure 5). The "annealed" material fractures primarily in an intergranular way, whereas the fracture surfaces of samples of the "hot-rolled" and "cold-rolled" material classes show mainly transgranular fractures. One sample of the "hot-rolled" material has been the subject of a detailed fracture surface analysis. This analysis revealed that the fracture behaviour is up to a very high percentage transgranular. Figure 5 also gives an impression of the crack path propagation. For the "annealed" material, the crack path is very straight, as expected, due to the macroscopic stress distribution caused by the striker impact. For both the "hot-rolled" and "cold-rolled" materials, the crack starts in a straight manner but is then deflected. This deflection of the main crack cannot be explained by the macroscopic stress distribution and must thus be caused by microstructural features. For the "cold-rolled" material and in particular for an L-S oriented sample, the branching of the main crack is most pronounced.

	Mat1-rxx („annealed")	Mat1 („hot-rolled")	Mat2 („cold-rolled")

L-S orientation

600°C (873 K) — striker, crack start; 600°C (873 K) — 50 µm

300°C (573 K); 300°C (573 K) — 50 µm

100°C (373 K); 100°C (373 K) — 50 µm

T-S orientation

600°C (873 K); 600°C (873 K) — 50 µm

400°C (673 K); 400°C (673 K) — 50 µm

200°C (473 K); 200°C (473 K) — 50 µm

Figure 5. Fractured surfaces of samples from the brittle regime (SEM).

Figure 6 gives an overview of the BDT temperatures and their anisotropic manifestation for all the material classes assessed. Furthermore, the diagram shows a result of the work from Németh et al.: the BDT temperature of UFG tungsten foil with a thickness of 100 µm tested in the L-S direction is at 77 K [29]. When comparing the results of both studies, it is important to take into account that the strain rates of the UFG tungsten foil test campaign were several orders lower (3×10^{-3} to 3×10^{-6} 1/s) than the strain rate of the tests presented in this paper (267.9 1/s).

The work of Németh et al. leaves the question open whether the BDT temperature decreases continuously through cold-rolling, or if a decrease of the BDT temperature requires a UFG microstructure. Here we show that the BDT temperature decreases continuously, at least for the L-S and T-S directions.

Figure 6 also provides the opportunity for a rudimentary view of the mechanisms controlling the BDT. It is popularly believed that screw dislocation motion proceeds via the nucleation of kink-pairs (steps on the dislocation line) and their subsequent lateral relaxation. Furthermore, the thermally-activated nature of the screw dislocation glide can be explained by the thermally activated nucleation of kink-pairs. In Ref. [29], the BDT temperature of UFG tungsten foil was found to be at 77 K. The authors assume that at such low temperatures the nucleation of kink-pairs is not very likely and that the BDT might thus not be controlled by the glide of screw dislocations, but by the glide of edge dislocations. The other extreme in Figure 6 represents the BDT of the "annealed" material (675°C, 948 K), where the thermally

activated nucleation of kink-pairs is likely. But how to deal with the intermediate BDT temperatures of the "hot-rolled" and "cold-rolled" materials? The reader is invited to consider whether or not these materials may benefit from (i) an enhanced nucleation of non-screw dislocations or (ii) an enhanced nucleation of kink-pairs. We assume that the BDT is still controlled by the glide of screw dislocations and that the decrease of the BDT temperature is related to the availability of dislocation sources.
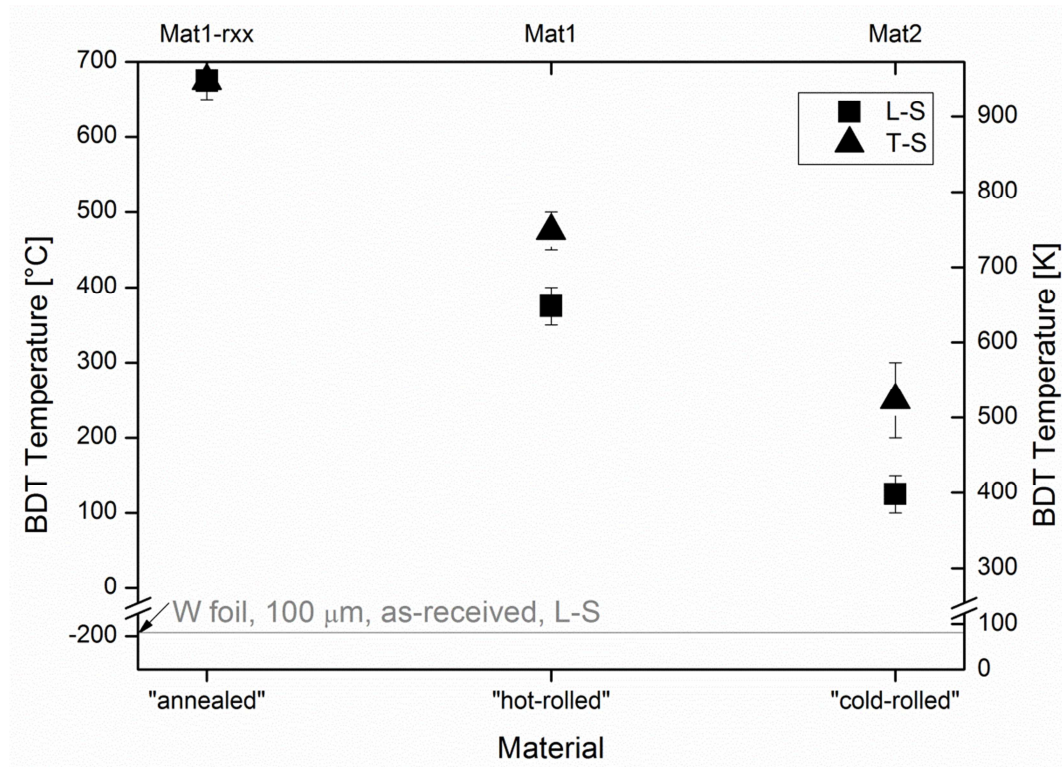

Figure 6. BDT temperature plotted against the material.

In order to increase the reliability of the results shown in Figure 3, several selected tests have been repeated. In particular, these are to confirm the BDT temperatures, thus tests at the highest temperature of the LSE and the lowest temperature of USE. Details can be found in Table 5.

Table 5: Results of the Charpy impact tests.

|		Mat1-rxx	Mat1	Mat2
BDT temperature [°C]	L-S	675	375	125
	T-S	675	475	250
BDT temperature [K]	L-S	948	648	398
	T-S	948	748	523
Samples tested to get the curve	L-S	8	8	12
	T-S	8	8	8
Experiments at the highest temperature of the LSE / the lowest temperature of the USE (confidential index)	L-S	1 / 1	1 / 1	4 / 3 (100% / 100%)
	T-S	1 / 1	3 / 2 (100% / 100%)	3 / 2 (100% / 100%)

In order to correlate the mechanical properties with the microstructure, a thorough analysis of the microstructure is required and is the subject of the next chapter.

4.2. Microstructure

### 4.2.1. Optical micrographs and hardness, HV0.1

In Figure 7 optical micrographs give a first impression of the microstructure of the "annealed", "hot-rolled" and "cold-rolled" materials.
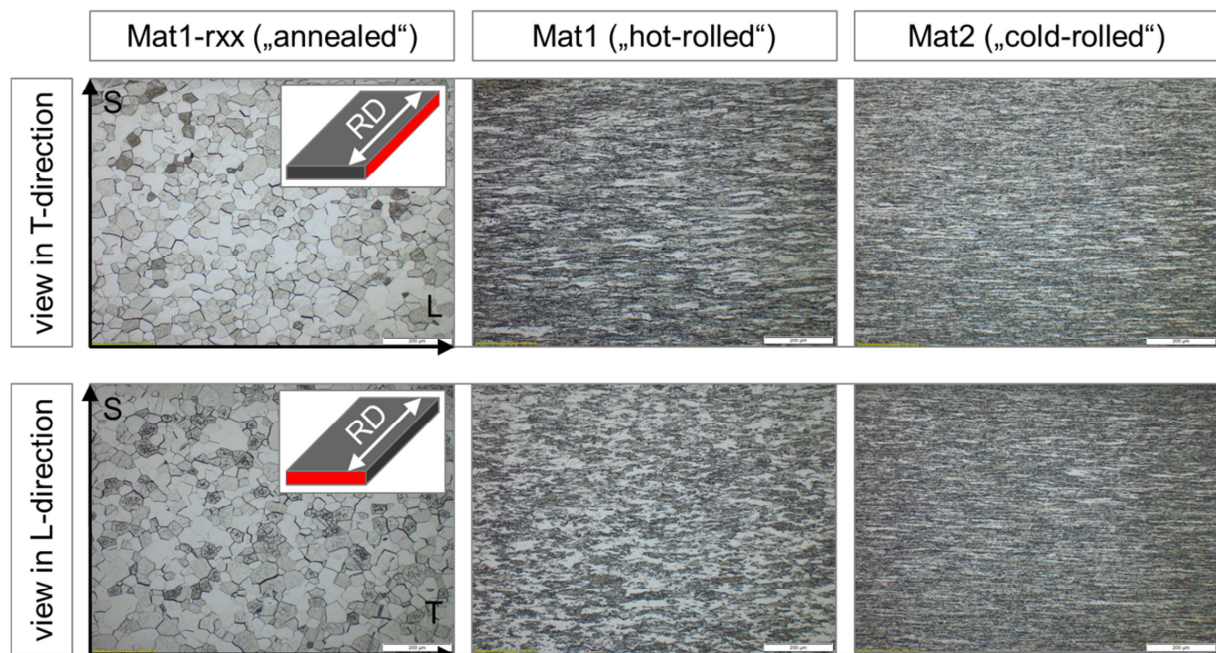
Figure 7. Optical micrographs showing cross sections with view in the T- and L-directions.

In Figure 8 the results of the hardness measurements (HV0.1) of the "annealed", "hot-rolled" and "cold-rolled" materials are plotted. The measurements were performed with indentation in both the L- and T-directions. Furthermore, the hardnesses are benchmarked against the hardness (HV0.1) of a tungsten single crystal (plane of indentation (110), 395 HV0.1) [34]. It can be found that the hardness (HV0.1) correlates with the amount of dissipated Charpy energy, E, in [J] according to

$$HV0.1 = 370 + 130 * E. \tag{5}$$
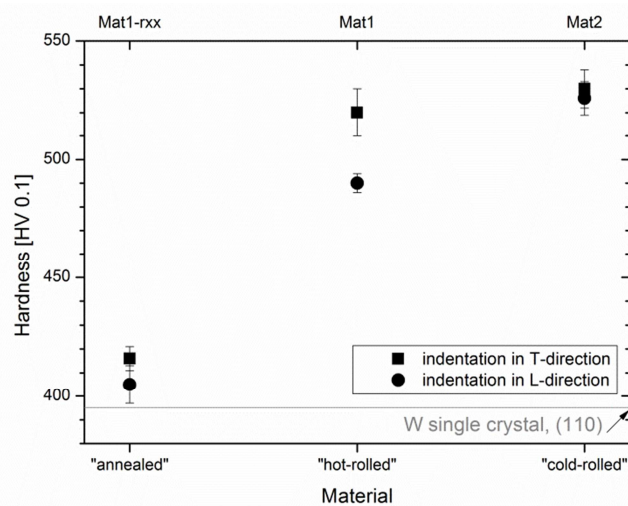
Figure 8. Hardness HV0.1 of the materials, measured in both L- and T-directions.

4.2.2. FIB-cuts

In order to get an impression of the microstructure of the "annealed", "hot-rolled", and "cold-rolled" plates, the materials were sliced using a focused ion beam (FIB). This technique in combination with the channelling contrast releases the microstructure and displays the grain distribution in and perpendicular to the rolling direction (Figure 9). Furthermore, Figure 9 gives an impression of the topology and homogeneity of the as-rolled surfaces. As the Charpy impact tests were designed in such a way that the crack starts at the as-rolled surface (the striker hits the eroded surface), the surface quality is an issue. For all materials the surface quality looks similar, which confirms the measurements of the roughness (R_a was measured to be about 1.5 μm for all materials; see Table 4).
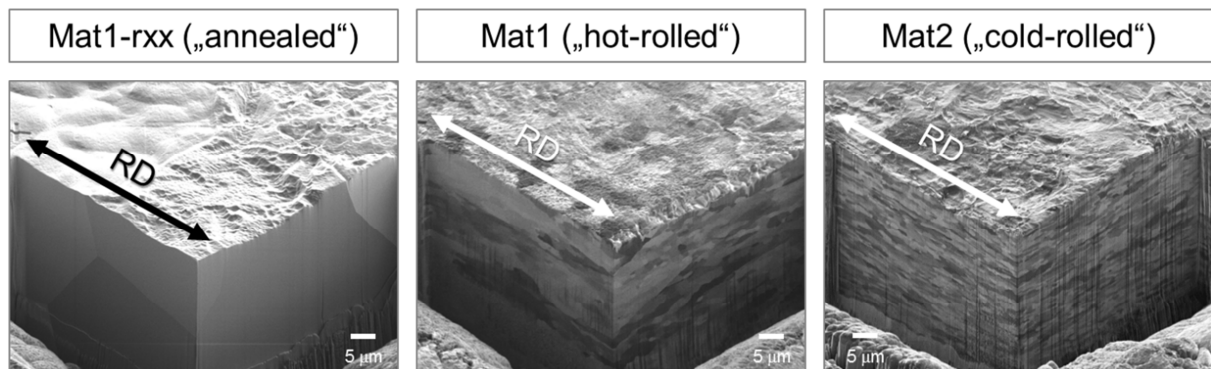
Figure 9. Material cut by FIB releasing the microstructure. The channelling contrast gives an impression of the grain size distribution. Furthermore, the surface quality can be estimated.

4.2.3. EBSD analysis

Using the EBSD data, the grain size and the crystallographic texture were calculated.

Figure 10 displays the IPFs of the "annealed", "hot-rolled", and "cold-rolled" materials. The mapping has an area of 140 μm by 140 μm (200 nm step size). Misorientations exceeding 15° were considered as HAGBs and are highlighted in black. Misorientations between 5° and

15

15° were considered as LAGBs and are highlighted in white. The IPFs reveal a significant reduction in grain size through hot- and in particular through cold-rolling.

The crystallographic texture of the "hot-rolled" and "cold-rolled" material represented by $\varphi_2 = 45°$ ODF sections can also be found in Figure 10. The rotated cube {100}<110> component with a spread along the α-fibre (<110> || RD) characterizes the texture of both the "hot-rolled" and the "cold-rolled" material. The γ-fibre (<111> || ND) orientations are less pronounced. The maximum ODF intensities are similar for both materials.
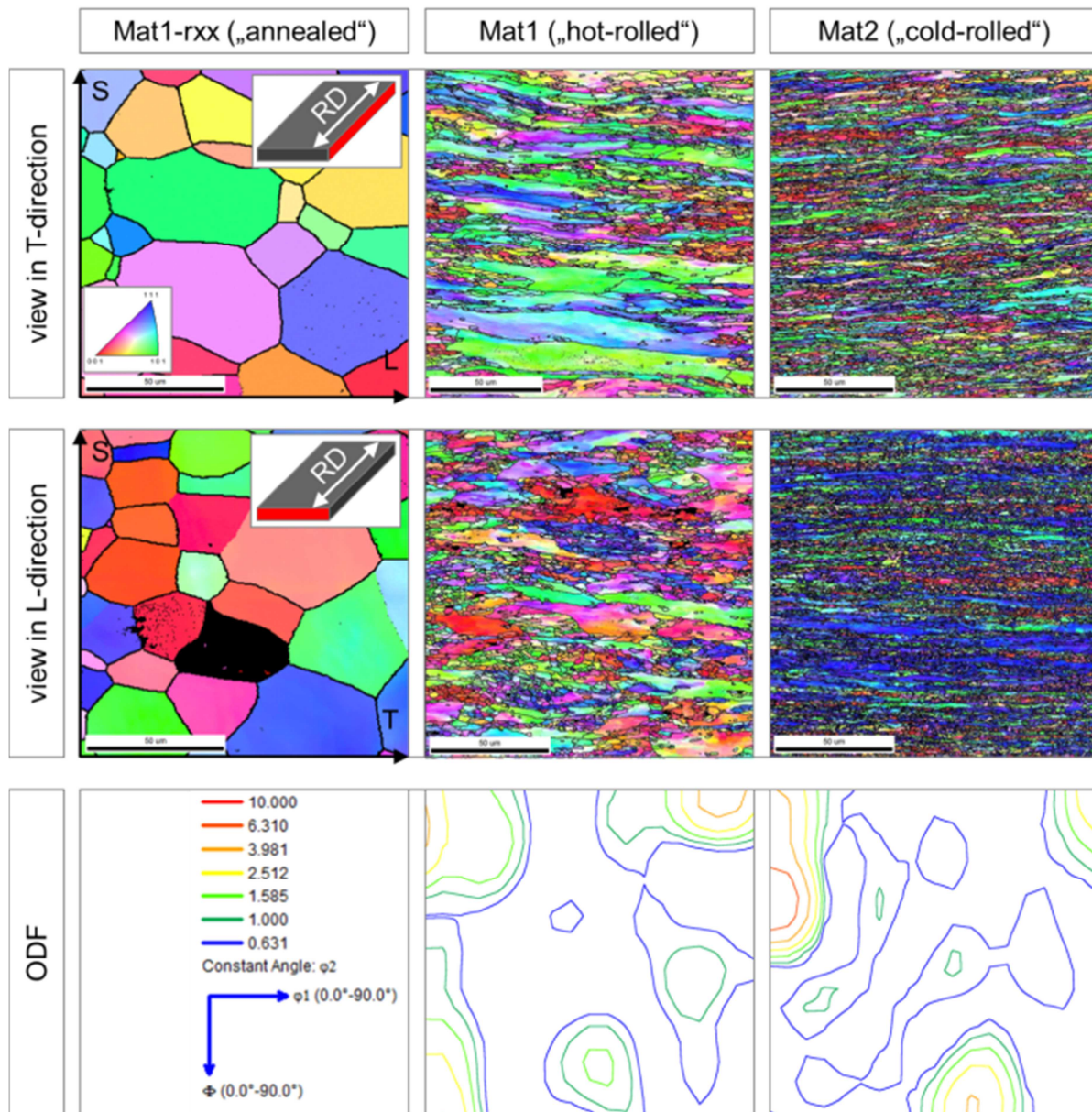
Figure 10. SEM analyses of the "annealed", "hot-rolled", and "cold-rolled" materials. From the top to the bottom: inverse pole figures (IPF), with HAGBs highlighted in black; textures of the "hot-rolled" and "cold-rolled" materials represented by $\varphi_2 = 45°$, and ODF sections (maxima are given in multiples of a random distribution).

In order to realize a profound basis for a microstructure-BDT-temperature correlation, a quantitative description of the grain size and grain shape is essential. Thus the IPFs from Figure 10 were used to evaluate the median grain sizes of the "annealed", "hot-rolled", and "cold-rolled" materials. This evaluation makes use of the line intersection method and only HAGBs were considered. The measured grain sizes can be found in Figure 11. The grain sizes in the T-direction result from the IPF with the view in the L-direction, and the grain sizes

in the L-direction result from the IPF with the view in the T-direction. The grain size in the S-direction was derived from an IPF with a view in the T-direction and from an IPF with a view in the L-direction.
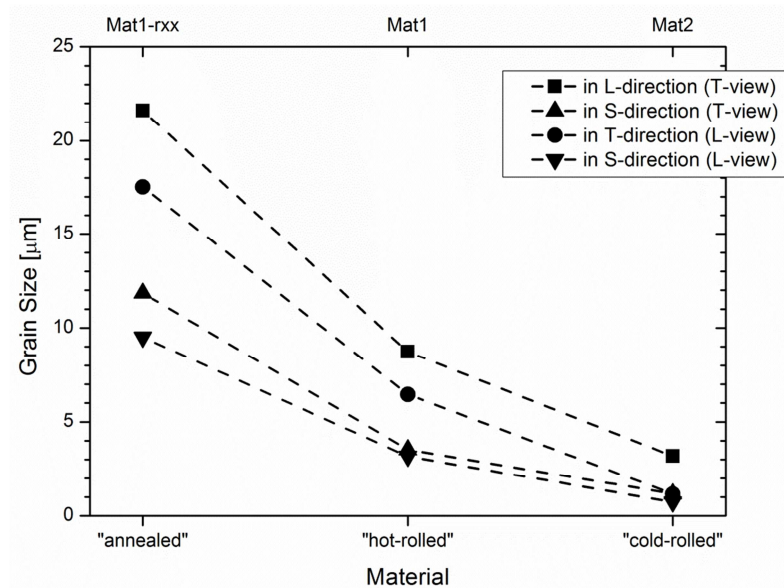
Figure 11. Median grain size in the L-, T-, and S-directions of the "annealed", "hot-rolled", and "cold-rolled" materials measured by the line intercept method. The grain size in the S-direction was measured both on a cross-section with a view in the L-direction and on a cross-section with a view in the T-direction.

For the purpose of a more detailed view on the LAGBs distribution, an area of 40 μm by 30 μm (30 nm step size) was analysed. The IPFs, grain boundary maps and the KAM maps are shown in Figure 12. The analyses were done with views in both the T- and L-directions. The IPFs of the "hot-rolled" and "cold-rolled" material, in particular those with a view in the T-direction, give an impression of elongated grains. The grain boundary maps (HAGBs highlighted in black, LAGBs highlighted in red) display a very pronounced subgrain structure. So, particularly for the cold-rolled material, the microstructure is characterized by a high number of low misorientation angles. Furthermore, by taking into account that the LAGBs are defined as misorientations between 5° and 15°, it is possible to estimate how the microstructure might be further subdivided by boundaries with misorientations smaller than 5°.
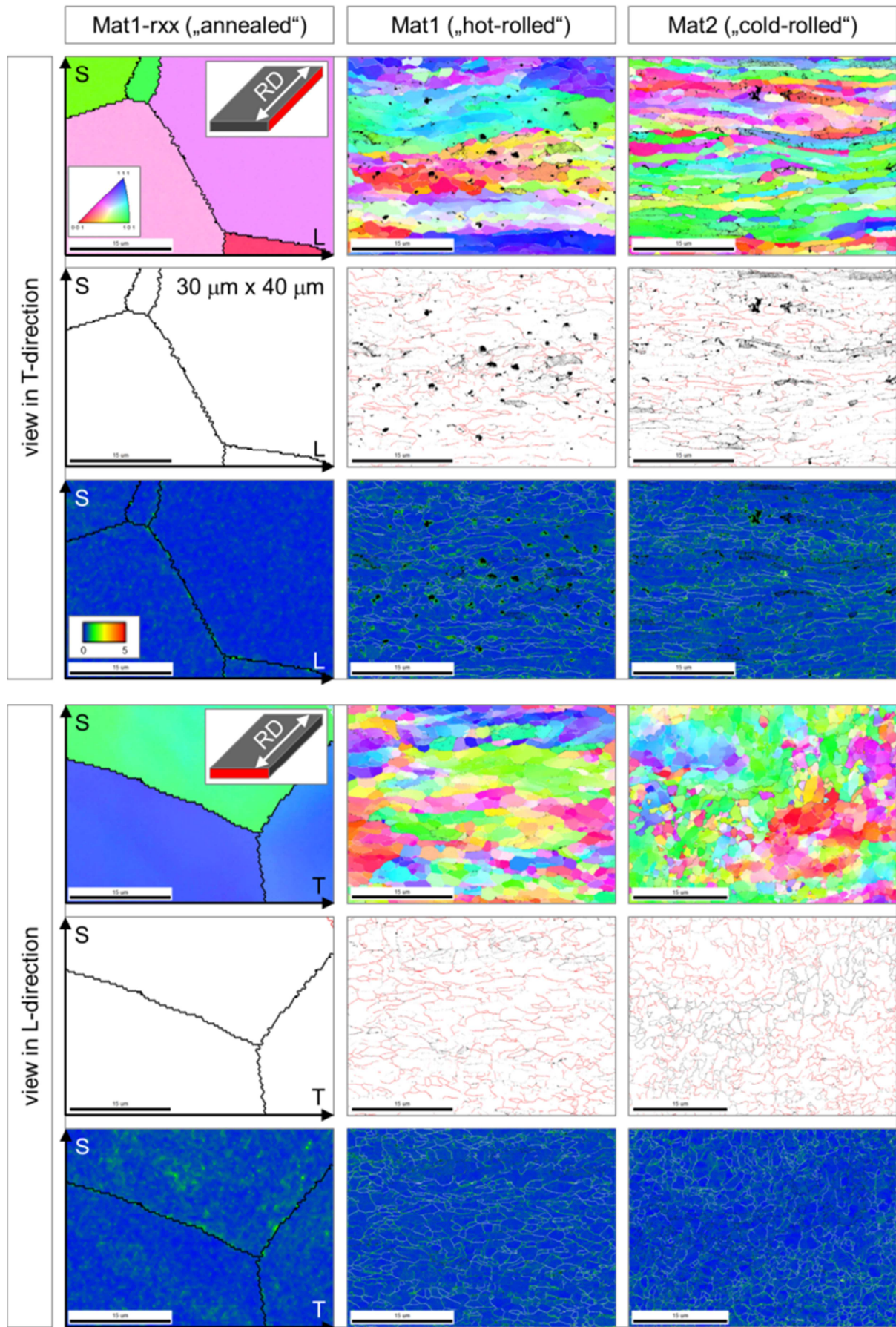
Figure 12. SEM analyses of the "annealed", "hot-rolled", and "cold-rolled" materials. From the top to the bottom: grain size distribution and orientation, (ii) grain boundary maps, and (iii) kernel average misorientation maps.

An overview of the distribution of the misorientation angle can be found in Figure 13, where the number fraction is plotted against the misorientation angle. The black line represents the microstructure of the "hot-rolled" material, which has a BDT temperature of 375°C (648 K), whereas the grey line shows the misorientation distribution of the "cold-rolled" material, which has a BDT temperature of 125°C (398 K).

Comparing both distribution plots it can be noted that the number of HAGBs increases through cold-rolling. According to this finding the decrease of the BDT temperature through cold-rolling might be correlated to the increase of the number of HAGBs. However Figure 13 does not show any distribution of misorientations in the range of 0° - 2° with a reliable accuracy. So no conclusion about the misorientation distribution in this misorientation range can be drawn.
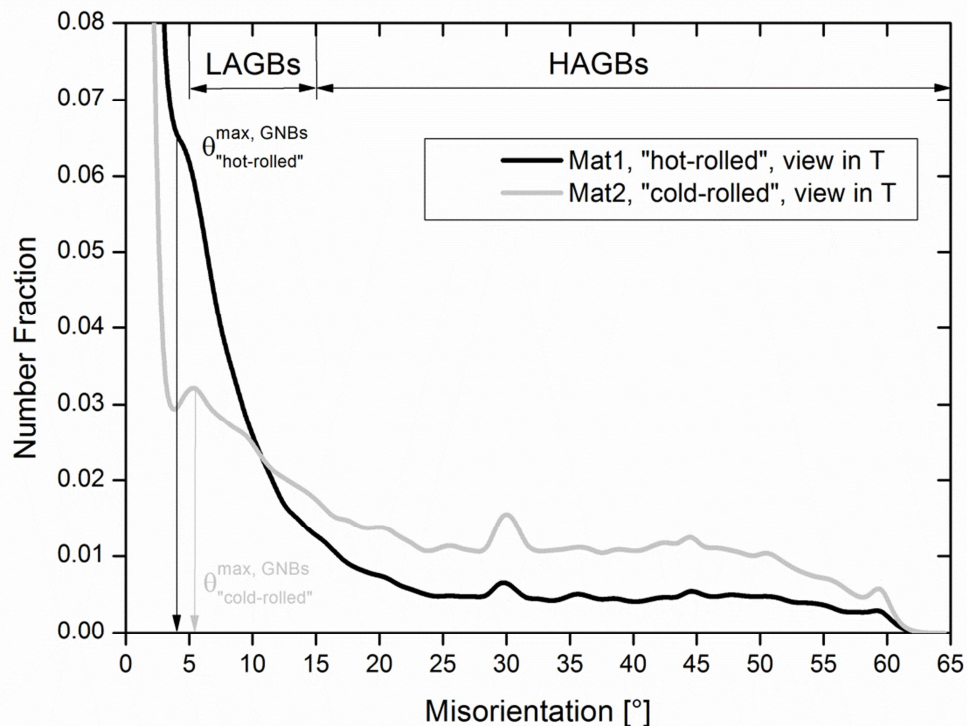
Figure 13. Distribution of the misorientation angle of the "hot-rolled" and "cold-rolled" materials.

During hot- and cold-rolling, dislocation structures develop with dislocation boundaries separating regions of different orientations [35]. These deformation-induced dislocation boundaries can be separated into two groups: (i) the geometrically necessary boundaries (GNBs) and (ii) incidental dislocation boundaries (IDBs). Figure 13 displays the evolution of the maximum misorientation angle, θ^{max}, of the geometrically necessary boundaries. As expected the maximum misorientation angle increase with subsequent rolling. This behaviour has also been reported for molybdenum by Mrotzek et al. [36]. The maximum misorientation angle for the incidental dislocation boundaries is expected to be in the range of approximately $0° < \theta^{max} < 1.5°$ and is thus below the resolution limit of the EBSD measurement. So no conclusion about the evolution of the maximum misorientation angle, θ^{max}, of the incidental dislocation boundaries can be drawn.

The KAM maps in Figure 12 show no significant increase of average misorientation inside the grains. However, for a reliable statement on the interior of the grains, TEM analyses are essential and are the subject of the next section.

4.2.4. TEM analyses

The aim of the TEM analyses is to provide a detailed view of the dislocation structure of the "annealed", "hot-rolled", and "cold-rolled" materials. In particular the TEM analyses should reveal the nature of the dislocation boundaries (IDBs, GNBs), as well as their distribution.

Figure 14 shows TEM bright field images of the microstructures of the assessed tungsten plates. The rolling direction is from bottom to top. All images provide a view in the T-direction. From the "annealed" material only one image is presented as any higher magnification does not provide any further information. The "hot-rolled" and "cold-rolled" microstructures are presented with three magnifications: (i) an overview, (ii) a magnification to estimate the dislocation boundary distribution as well as (iii) a detailed view of selected dislocation boundaries.

The overview micrographs confirm the results from the EBDS analyses, which show a decrease of grain size through cold-rolling. Furthermore it can be stated, that in general the interior of regions separated by low and high angle boundaries contains only a small amount of free dislocations. So it is worth to focus on the nature and the character of the dislocation boundaries.

A statement about the densities of the dislocation boundaries of the "hot-rolled" and the "cold-rolled" microstructure is not possible as dislocation boundaries can be found in both microstructures. It may be that the number of dislocation boundaries increases through cold-rolling, but this is only a subjective evaluation.

The images of the highest magnification show selected dislocation boundaries. It can be noticed that the dislocations forming the dislocation boundaries are highly curved. Thus the dislocation boundaries can be interpreted as incidental dislocation boundaries. Due to the highly curved morphology of the incidental dislocation boundaries, the IDBs are necessarily of mixed character, spanning the whole range of the of values of the dot product of the boundary normal, n, and the boundary rotation axis, l, from pure tilt (only edge dislocations) to pure twist (only screw dislocations). The dislocations forming the IDBs are loosely netted. It may be assumed that such small angle nets can act directly as Frank-Read sources. Figure 14 allows a comparison of the incidental dislocation boundaries of the "hot-rolled" and "cold-rolled" materials. Qualitatively it is observed that the curvature of the dislocations forming the boundary increases through cold-rolling.

	Mat1-rxx („annealed")	Mat1 („hot-rolled")	Mat2 („cold-rolled")
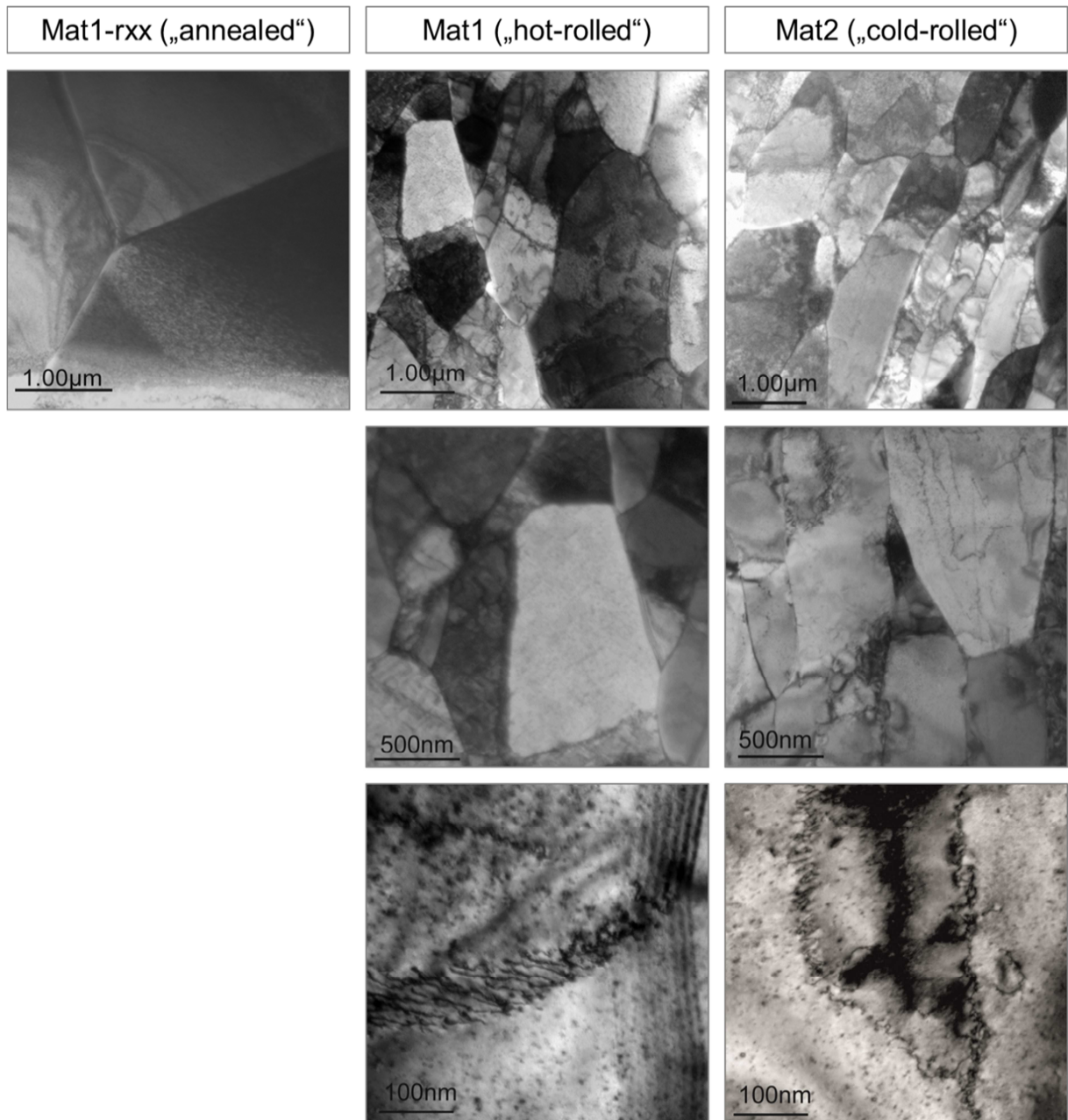
Figure 14. TEM bright field micrographs providing a detailed view of the dislocation structure.

Table 6 provides a summary of the analyses of the microstructure by means of quantitative characteristics such as hardness, grain size and grain shape. With regard to a microstructure-BDT-temperature correlation, the following chapter addresses the question: Is there a correlation between microstructural features and the BDT temperature?

Table 6: Summary of analyses of the microstructure.

		Mat1-rxx	Mat1	Mat2
Hardness, HV0.1	indentation in T-direction	416 ± 5	520 ± 10	530 ± 8
	indentation in L-direction	405 ± 8	490 ± 4	526 ± 7
Mean grain size [µm]	in L-direction (measured on IPF with view in T-direction)	21.61	8.73	3.18

in T-direction (measured on IPF with view in L-direction)	17.53	6.46	1.16
in S-direction (measured on IPF with view in T-direction)	11.85	3.53	1.17
in S-direction (measured on IPF with view in L-direction)	9.51	3.17	0.73

5. Discussion

This section is organized into two parts. In the first part, a phenomenological-analytical approach is used to correlate the microstructure with the BDT temperature and to describe both (i) the shift of the BDT for the "annealed", "hot-rolled", and "cold-rolled" material classes and (ii) the differences of the BDT temperature for L-S and T-S oriented samples. In the second part, a mechanism-based approach is used to discuss again both (i) the shift of the BDT for the assessed material classes and (ii) the difference in material responses depending on the sample orientation (L-S and T-S).

5.1. Phenomenological-analytical approach

The relationship between strength and mean grain size is well known. The yield strength, σ_y, is given by the classic Hall-Petch relation

$$\sigma_y = \sigma_0 + k_y * d^{-n} \tag{6}$$

where σ_0 is a constant stress of uncertain origin, k_y is a material constant, d is the mean grain size, and the exponent n is approximately 0.5. The Hall-Petch effect is one of the oldest size effects reported in literature (in 1951 [37] and 1953 [38] respectively). Nevertheless, an in-depth understanding of the microstructural mechanisms still does not exist yet, and there are several different theories (theory of dislocation pipe-up, work hardening theories, or grain boundary source theories) that try to explain the Hall-Petch relation [8,39].

By analogy to Eq. 6, one may also try to establish a constitutive equation for the BDT temperature and the mean grain size

$$T_{BDT} = T_0 - k_{BDT} * d^{-n} \tag{7}$$

where T_{BDT} is the BDT temperature, T_0 is a constant temperature, k_{BDT} is a coefficient, d is the mean grain size, and the exponent n is approximately 0.5 [40,41].

Eq. 7 has proved to be useful in the steel community. It may also be useful to describe the shift of the BDT for the "annealed", "hot-rolled", and "cold-rolled" material classes when d is the mean grain size in the S-direction. However, Eq. 7 cannot explain the different BDT temperatures of the samples (of one material class) oriented in the L-S and T-S directions. An equation that considers the anisotropy of the BDT should therefore consider also the aspect ratio of the mean grain size. Hence, we expand Eq. 7 with the mean grain size aspect ratio, d_2/d_1, to

$$T_{BDT} = T_0 - k_{BDT} * (d_2/d_1)^m * d_1^{-0.5} \tag{8}$$

22

where the exponent m is approximately 1, d_1 is the grain size in the expected direction of crack propagation, and d_2 is the grain size in the direction normal to the expected crack plane. For example, the L-S specimen crack propagation is in the S-direction (and thus d_1 is the grain size in the S-direction) and the direction normal to the expected crack plane is the L-direction (and thus d_2 is the grain size in the L-direction).

The verification of Eq. 8 can be found in Figure 15, where the BDT temperature is plotted against $d_2/d_1 * d_1^{-0.5}$. Figure 15 also shows a best fit straight line from which T_0 and k_{BDT} can be derived to

$$T_{BDT}\ (\dot{\varepsilon} = 267.9\ 1/s) = \ 1083\ K - \ 280\ K\ \mu m^{0.5} * d_2/d_1 * d_1^{-0.5}. \tag{9}$$

(or

$$T_{BDT}\ (\dot{\varepsilon} = 267.9\ 1/s) = \ 1083\ K - \ 8.85\ K\ mm^{0.5} * d_2/d_1 * d_1^{-0.5}. \tag{10}$$

respectively). This equation represents the mechanical behaviour of 99.97 wt % W tested at an outer-fibre strain rate of 267.9 1/s. It can be regarded as a type of master curve that allows determination of the BDT temperature of samples in other orientations such as the S-L or L-T orientations. The predictive power of this master curve has now to be verified by systematic tests. These tests have to take into account that Eq. 7 is logarithmic rather than linear (see section: "Comparison with bcc steels and molybdenum (Mo)"). Similar to the Hall-Petch relation, Eqs. 8, 9 and 10 are based on experimental measurements only and have the character of a phenomenological description.
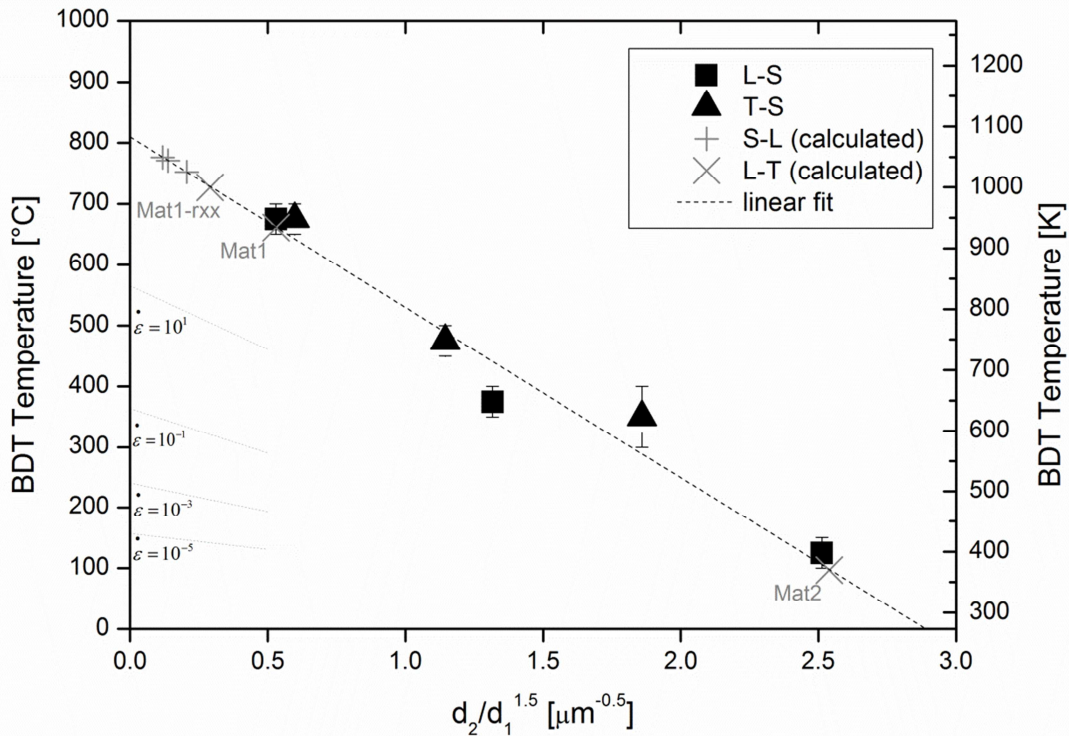

Figure 15. Empirical correlation between the grain size / grain shape and the BDT temperature. The dotted lines represent the calculated BDT temperatures (calculated according to Eq. 9) at different strain rates. For the calculations, an activation energy for the BDT, Q_{BDT}, of 1.05 eV is used.

The connection between cold-rolling and the BDT temperature can be understood on the basis of a Yoffee-type diagram (Figure 16). This diagram displays a cleavage resistance stress, σ_F, (also known as brittle fracture stress) and a crack tip stress, σ_T, which is defined as the peak tensile stress in the process zone of a crack tip in an elastic–plastic material. This peak tensile stress, σ_T, scales with the yield stress, σ_y, which is known to be rate-dependent for bcc materials. It follows that as long as the crack tip stress, σ_T, is below the cleavage resistance stress, σ_F, the material yields before cleavage and the material behaviour is ductile [41,42]. Thus the BDT temperature can be quantitatively interpreted as a result of the competition between the flow stress and the cleavage resistance stress of the material.

From Figure 16 it appears that the rate-dependence of the yield stress, σ_y, is directly linked with the rate-dependence of the BDT temperature. Furthermore, it is well established that cold-rolling increases the yield stress (grain boundary hardening, dislocation hardening), which would lead to an increase of the BDT temperature. However, cold-rolling also increases the cleavage resistance stress, σ_F. The effect on the cleavage resistance stress, σ_F, is ordinarily larger, with the result that the BDT temperature decreases.
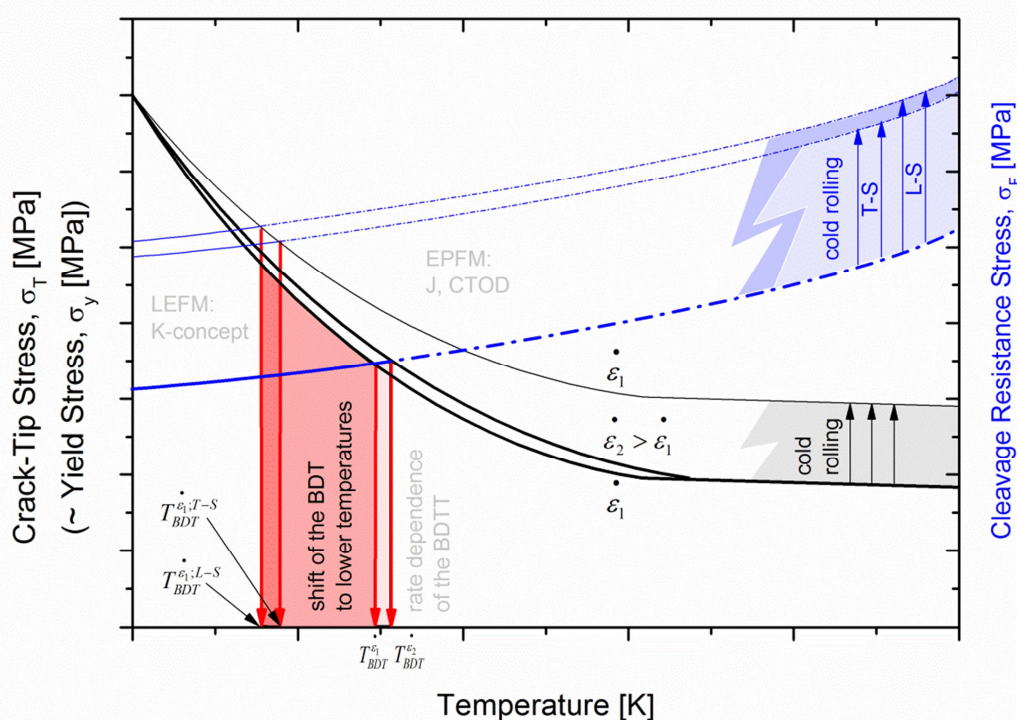
Figure 16. Yoffee-type diagram. The BDT occurs when the crack tip stress, σ_T, exceeds the cleavage resistance stress, σ_F. Cold-rolling raises both σ_T and σ_F, but the effect on σ_F is ordinarily larger, with the result that the BDT temperature decreases.

Similar to the Hall-Petch relation, the diagram in Figure 16 displays a phenomenological-based description of the relation between the BDT temperature and cold-rolling. In the next section, a mechanism-based approach is discussed, addressing the following main questions:

(1) What are the microstructural mechanisms that increase the cleavage resistance stress, σ_F?

24

(2) How does cold-rolling increase the cleavage resistance stress, σ_F?

## 5.2. Mechanism-based approach

The mechanism-based discussion addresses issues like (i) microcracking (as well as branching of the main crack and crack bridging effects), (ii) crystallographic texture, (iii) the role of dislocations, (iv) impurities, and (v) sinter pores.

5.2.1. Microcracking (as well as branching of the main crack and crack bridging effects)

For the following discussion, it is of utmost importance to make certain that the macroscopic irreversible deformation of the Charpy impact samples of the ductile regime (Figure 4) is based on the dislocation activity only, and that the deformation is not supported by or based on microcracking. The detection of microcracks can be done by, e.g., the infiltration technique, by scanning acoustic microscopy, or SEM analysis. In Figure 17, a SEM analysis of the outer fibre and inner fibre region of a Charpy impact test sample of the "cold-rolled" material class, tested in the L-S orientation at 150°C (ductile regime) gives an impression of the deformed microstructure. The SEM analysis was designed to detect microcracks; however, no microcracks were found. Therefore it can be derived that the macroscopic irreversible deformation of the Charpy impact samples of the ductile regime is most likely caused by plastic deformation only, so the role of dislocations appears to be one of the most important aspects when discussing the shift of the BDT temperature to lower temperatures through cold-rolling.

Nevertheless, the situation might look different for a severe cold-rolled microstructure, like that of a tungsten foil. Several authors have reported on the exceptional mechanical properties of cold-rolled tungsten foils. Wei and Kecskes [43] presented stress-strain curves of cold-rolled tungsten foils. Their results of tensile tests at room temperature (RT) show up to 8 % plastic strain. Németh et al. [29] evaluated the BDT temperature of ultrafine-grained tungsten foil and determined a BDT temperature of about 77 K. Furthermore, Pippan [44,45] showed crack growth resistance curves (R-curves) of pure tungsten foils with a thickness of 160 μm and determined a RT fracture toughness, K_{IQ}, of 95 MPa m$^{1/2}$ in the L-T direction and of 65 MPa m$^{1/2}$ in the T-L direction (at a crack extension of Δa = 200 μm and an initial crack length of a = 9 mm, a/W = 0.5, single edge notched tension (SENT) specimens). It seems very likely that the R-curve behaviour is caused by crack bridging effects, similar to those known from silicon nitrides (Si_3N_4) (stage I: formation of elastic bridges; stage II: partially debonded elastic bridges; stage III: fully debonded frictional bridges) [46].
So, in general, it is worth discussing exceptional mechanical properties against the background of microcracking, branching of the main crack and crack bridging effects. However, for the materials assessed in this study, the deformation of the Charpy impact samples of the USE level is very probably caused by plastic deformation only.
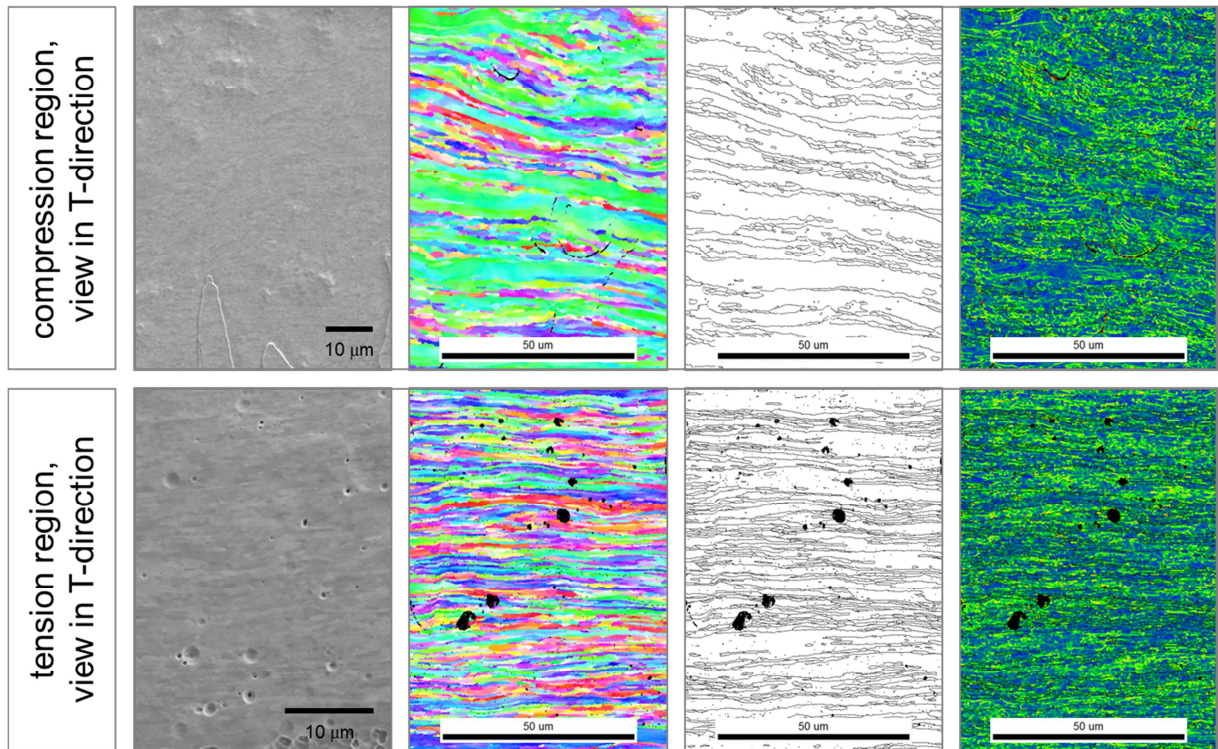
Figure 17. Sample: L-S, "cold-rolled", tested at 150°C. On both the most stressed compression and the most stressed tension region, no microcracks are observed. This result emphasises the role of dislocations. From left to right: SE, IPF, HAGBs, KAM.

5.2.2. Crystallographic texture

Indeed, the BDT temperature is a function of the crystallographic texture. Table 7 displays the results of measurements of BDT temperatures of tungsten single crystals. There, depending on the cleavage plane and the crack front direction, the BDT temperature occurs in an interval of 100 K. This value of 100 K gives an impression of how much texture might affect the BDT temperature also for polycrystalline tungsten materials.

The ODFs of the materials assessed within this study show that the differences in the texture of the "hot-rolled" and "cold-rolled" materials are weak. Both the texture components and the intensities are similar (Figure 10). So it can be concluded that texture has only a minor impact on both (i) the shift of the BDT for the "annealed", "hot-rolled", and "cold-rolled" material classes and (ii) the differences of the BDT temperature for L-S and T-S oriented samples.

The situation might look different for severe unidirectional cold-rolled tungsten sheets like a tungsten foil. Usually, unidirectional rolling leads to a strengthening of the main texture component, which for molybdenum and tungsten is a weak α-fibre with a maximum at the rotated cube component {100}<110> [47]. This means that the preferred cleavage planes of tungsten, the {100} planes, (i) form an angle of 45° with the rolling direction (45° embrittlement [48]) and (ii) promote the splitting of the sheets (S-L, S-T crack systems, normal of the crack plane is the S-direction).

Table 7: BDT temperatures and fracture toughness at RT of pure tungsten. Data of tungsten single crystals (SX) are from Ref. [14]. The crack system is defined as crack plane and crack front direction. The loading rate was $\dot{K} = 0.1 \pm 0.02\ MPa\ m^{1/2}s^{-1}$. Data of polycrystalline tungsten are from Ref. [49] (W as-sintered) and from Ref. [29,44,45] (W foil).

W material	W SX, {100}<010>	W SX, {100}<011>	W SX, {110}<001>	W SX, {110}<1$\bar{1}$0>	W as-sintered	W foil

BDT temperature [K]	470	370	430	370	-	77 (L-S orientation, $\dot{\varepsilon} = 3 * 10^{-2}\,s^{-1}$
Fracture toughness at RT [MPa m$^{1/2}$]	8.7 ± 2.5	6.2 ± 1.7	20.2 ± 5.5	12.9 ± 2.1	5.1	70 (L-T orientation)

5.2.3. Impurities, micropores and sinter pores

Due to the complex interaction between impurities, micropores and sinter pores, these issues are discussed in the same context. The solubility of interstitial elements in tungsten, such as hydrogen (H), nitrogen (N), oxygen (O), silicon (Si), and carbon (C) at RT is very low (< 0.1 µg/g) and the grain boundary strength can be significantly weakened by impurities segregated at the grain boundaries [34].

The fracture behaviour of polycrystalline tungsten has often been discussed with respect to the influence of impurities. In particular, the impact of grain boundary impurities on the low cohesion of tungsten grain boundaries has been the subject of several studies [50,51,52,53]. A comprehensive study can be found in Gludovatz et al. [54], who came to the conclusion that for the analysed tungsten materials, grain boundary impurities do not have a significant influence on the fracture resistance of the boundaries.

With regard to the material assessed within this study one may argue that through grain refinement the density of grain boundaries increases and thus the density of impurities at the grain boundaries decreases. Furthermore, one may assume that through cold-rolling low-energy sites (dislocation tangles) are formed. Segregation of interstitials to these sites may increase the grain boundary strength and thus increase ductility [34]. So a further explanation for the increase of the cleavage resistance stress through cold-rolling might be the decrease of the impurities concentration at the grain boundaries.

The influence of micropores and sinter pores on the intergranular fracture toughness of tungsten has been less intensively investigated. However, initial indications can be found in Hoffmann and Wesemann [55], who compared the evolution of the porosity for standard pure tungsten with a metallic purity of > 99.97 wt % W and ultrahigh purity tungsten with a metallic purity of > 99.998 wt % W. One may assume that through cold-rolling the former sinter pores align in a preferred direction, which is perpendicular to the expected macroscopic crack plane. This mechanism may increase the cleavage resistance stress. Tests on samples oriented in the S-L and S-T directions can shed some light on this issue.

At the beginning of the Discussion section we expanded Eq. 7 with the mean grain size aspect ratio $(d_2/d_1)^m$ in order to give a suitable description of the different BDT temperatures for samples tested in the L-S and T-S directions. In Eq. 8 we assumed that $m = 1$. One may argue that with increasing metallic purity and with decreasing size of the sinter pores of the tungsten sintered ingot, m is heading towards 0 (and, of course, $T_0(\dot{\varepsilon})$ and k_{BDT} decrease as well). In this case, we came back to Eq. 7, which has been approved well for describing the relation between the BDT temperature and the grain size for ferrous steels.

As the "hot-rolled" and "cold-rolled" materials showed primarily transgranular fracture we do not think that impurities effects are the most important parameter responsible for the decrease of the BDT temperature.

5.2.4. Role of dislocations – dislocation density, nature of dislocations, dislocation boundaries

The question of what mechanisms increase the cleavage resistance stress is still open. However, the discussion so far emphasises the necessity to focus on the role of dislocations. An initial impression of the role of dislocations can be derived from experimental results obtained from pre-deformed tungsten single crystals as presented in Ref [9]. There, the importance of the number of active dislocation sources is discussed.

Furthermore, Lassner et al. [34] talked about "ductile tungsten" and a pronounced decrease in the BDT temperature as a result of cold-working. There, the behaviour was explained, among other, by the formation of a large amount of edge dislocations, which move rather easily during deformation and thus provide a better ductility.

A further indication can be found in the work of Cheng et al. [56]. There, the authors explain the decrease of the strain rate sensitivity with decreasing grain size of molybdenum as follows: with decreasing grain size, the density of mixed and edge dislocations increases, while the density of screw dislocations decreases. If such behaviour is also true for cold-rolled tungsten plates, then the increase of the density of mixed and edge dislocations might be a further reason for the increase of the cleavage resistance stress.

With regard to the material assessed within this study, it is important to say that for the "hot-rolled" and "cold-rolled" materials we found low-angle boundaries that we identified as IDBs. It is well known that in low-angle boundaries the segments of dislocation networks forming the boundary can act as Frank-Read or Bardeen-Herring sources [8]. So the availability of such dislocation sources might be a further reason for the decrease of the BDT temperature. However, for a reliable conclusion about the dislocation density, the nature of dislocations, the characteristic of the low-angle boundaries (IDBs, GNBs), their misorientation and their performance as dislocation sources, further electron microscopy analyses are essential.

5.2.5. Role of dislocations – grain boundaries (HAGBs) acting as dislocations source vs obstacle

There is a controversial discussion about the impact of grain boundaries on BDT temperature. In Lassner et al. [34], there is a comparison of the stress-strain curves of tungsten single crystals and polycrystalline tungsten material. From these curves, Lassner et al. concluded that the presence of grain boundaries significantly lowers the BDT temperature and remarkably degrades the low-temperature plastic properties of tungsten.

The situation looks different with regard to the work of Giannatassio et al. [24]. In their study, the authors compared the BDT of pre-cracked tungsten specimens by rate-dependent four-point bend tests. As the values of the BDT temperature were the same for pure single-crystals and polycrystalline tungsten (99.99 wt % W, mean grain size 3 μm), the authors came to the conclusion that dislocation motion near the crack tip is not significantly affected by the presence of grain boundaries.

Furthermore, Zeng and Hartmaier [27] modelled size effects on the fracture toughness of polycrystalline tungsten by means of dislocation dynamics. Their numerical experiments revealed that the fracture toughness decreases with grain size, because grain boundaries confine the plastic zone. Thus, the shielding dislocations pile-up at the grain boundary closest to the crack-tip, which causes high stresses in the neighbouring grain. This in turn can trigger the plastic yielding of that grain. Hartmaier brought forward the hypothesis that the activation energy for the BDT in a polycrystal should be related to the dislocation-grain-boundary-interaction energy (dislocation absorption/renucleation, activation of slip systems in the neighbouring grain) [28]. According to this, the BDT of fine-grained tungsten might neither be controlled by (i) dislocation nucleation, nor by (ii) dislocations glide, but by (iii) the absorption and renucleation of dislocations at the grain boundaries. So any correlation

between grain size and BDT temperature, rate-dependence of the BDT, and activation energy for the BDT, Q_{BDT}, should be discussed against the background of Hartmaier's interpretation.

Our results presented within this study provide a further contribution to this discussion; the BDT temperature decreases with grain size. Due to the different conclusions of the references mentioned above, further systematic studies seem to be essential to elucidate the role of grain boundaries on the BDT temperature. Such studies might then confirm that grain boundaries act as dislocation sources (e.g. boundary ledges provide sites for dislocation nucleation), which would provide a further explanation of the increase of the cleavage resistance stress with decreasing grain size.

5.2.6. The anisotropy of the BDT temperature

Up to now, we have provided assumptions to explain the shift of the BDT for the "annealed", "hot-rolled", and "cold-rolled" material classes. However, an explanation of the differences of the BDT temperature for L-S and T-S oriented samples of the same material class has not yet been discussed.
An explanation might look as follows: we assume grain boundaries to be the weakest link in the chain, and that the transgranular fracture toughness is significantly higher than the intergranular fracture toughness. Considering the preferred crack path on the macro level (crack penetrating in the S-direction), the density of grain boundaries aligned in the S-direction is higher for samples tested in the T-S direction than for samples tested in the L-S direction (Figure 18). This might explain why the cleavage resistance stress is higher for samples representing the L-S direction than for samples in the T-S direction. So the density of grain boundaries aligned in the direction of the preferred macroscopic crack direction might explain the L-S, T-S differences. However, as we observed no intergranular fracture for both "hot-rolled", and "cold-rolled" material classes, we think that this explanation is not convincing.

Another explanation considers the distribution of dislocation sources such as dislocation boundaries or grain boundaries and their anisotropic distribution that is established during rolling. The fact that dislocations can be emitted from boundaries has been shown in many investigations. For example, in low-angle boundaries the segments of dislocation networks forming the boundary can act as Frank-Read or Bardeen-Herring sources. Further possible sources are boundary ledges that provide sites for dislocation nucleation [8]. Assuming that boundaries perform differently as dislocation sources, then the anisotropic distribution of those dislocation sources might be another explanation for the different material responses of the L-S and T-S oriented samples.
The reader is invited to critically reflect on the general issue of the different material responses of rolled tungsten plates tested in (0°) and perpendicular (90°) to the rolling direction against this background (e.g. tensile test properties at room temperature [57]).
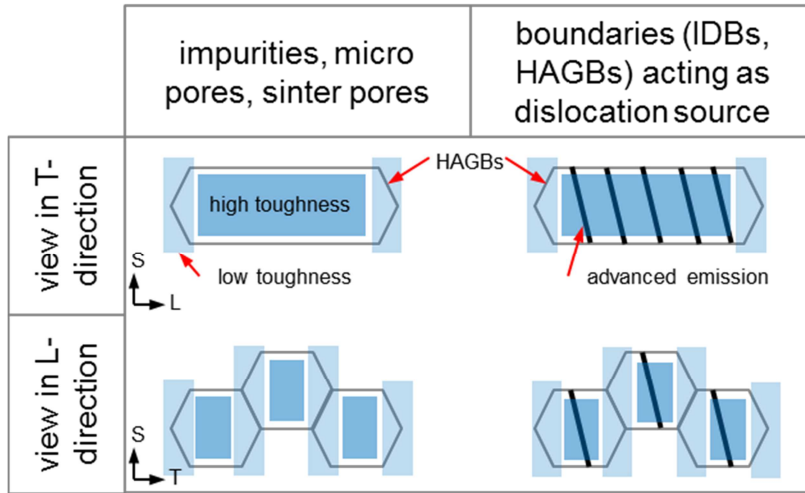
Figure 18. The different material response for L-S and T-S oriented samples might be explained by the anisotropic distribution of dislocation sources.

5.3. Comparison with bcc steels and molybdenum (Mo)

In the steel community, it is generally accepted that grain refinement of steels which show a BDT results in a decrease of the transition temperature [40,42,58,59]. Furthermore, it is generally accepted that fine-grained steels show an improved combination of strength and toughness compared with their corresponding coarse-grained counterparts. So grain refinement is the only strengthening mechanism that also increases toughness or decreases the BDT temperature [40,58].

The equation developed to relate the BDT temperature to grain size, d, is

$$\beta * T_{BDT} = \ln \beta - \ln C - \ln d^{-0.5} \tag{11}$$

where β and C are constants [60,61]. As the deviation of $\ln d^{-0.5}$ from the linear function $d^{-0.5}$ is not great over a limited grain size range, the function usually used is linear rather than logarithmic, giving an equation of the form

$$T_{BDT} = T_0 - k_{BDT} * d^{-0.5} \tag{12}$$

(see Eq. 7). Similar to the classic Hall-Petch relation for strength, a mechanism-based interpretation of the effect of grain size on the BDT temperature is controversial (model of crack re-orientation on HAGBs, Cottrell criterion) [40]. Gladman and Pickering comment that for Eq. 12 the nature of the grain boundary is most important and LAGBs should not be included in the $d^{-0.5}$ term [40].

The fracture behaviour of UFG α-iron (α-Fe) has been investigated by Song et al. [59], Inoue et al. [42], Hohenwarter and Pippan [62], and Gizynski et al. [63]. Both Song et al. [59] and Inoue et al. [42] discussed not only the effect of grain refinement on the shift of the BDT temperature but also the effect of "delamination". Delamination is defined as the branching of the main crack and leads to a decrease in the triaxiality of the stress state in the impact test sample. Both authors came to the conclusion that the BDT temperature is lower in the ultrafine-grained steel than in comparable coarse-grained specimens. However, Hohenwarter and Pippan [62] investigated the BDT temperature of α-Fe after equal-channel angular pressing (ECAP) and high pressure torsion (HPT). They found that the BDT temperature of severe plastic deformation (SPD) processed iron is higher than that of coarse-grained α-Fe. They assumed that this behaviour was related to intercrystalline cracking in as-SPD processed iron.

As branching of the crack (delamination) has also been observed in fracture experiments of deformed tungsten products (W rods, K-concept [25]; W rods and plates, Charpy [32,64]), the question of secondary cracks and their propagation is of utmost importance.

Finally, there is work on UFG α-Fe by Gizynski et al., who emphasised the role of dislocation density [63].

The results presented in this paper are consistent with results obtained for molybdenum. Eck and Pink reported on the effects of working on the BDT of molybdenum alloys. They observed that with progressive working the BDT temperature decreases. This behaviour was explained by the beneficial effects of dynamic strain ageing [65]. Similar results have been reported by Northcott, who compared the BDT temperature of recrystallized and hot- and cold-worked molybdenum [66].

5.4. Critical remarks

Our results are only of a preliminary character, as our study shows some weaknesses. The first critical point to mention here is the fact that the "cold-rolled" and "hot-rolled" plates are not made from one and the same sinter ingot. Of course, both plates fulfil the quality requirement of technically pure tungsten (> 99.97 wt % W) and both plates satisfy the specification of the supplier [30]. Nevertheless, the chemical composition is not identical for both plates. It is well known that the concentration of impurities has an impact on both the BDT temperature and the activation energy of the BDT. So it is up to the reader to evaluate the influence of the different chemical compositions of the "cold-rolled" and "hot-rolled" tungsten plates on the BDT temperature. Any ensuing investigation, however, has to consider this fact and work with material processed from one and the same sinter ingot.

Another critical aspect that has to be mentioned here is surface quality. Our tests were designed in such a way that the starting point of the crack is on the plate surface, which is in its as-received condition. We support this decision, as the quality of the surfaces of the tungsten plates was found to be homogeneous and satisfactory (Figure 9). Nevertheless, in a further study, we recommend polishing both the as-received and the spark eroded surfaces before testing.

A further serious issue that has to be addressed is statistics. Lassner and Schubert raised a critical note, saying that the identification of absolute values for the mechanical properties of polycrystalline tungsten is not appropriate as long as the microstructure cannot be precisely defined [34]. Therefore they proposed to regard data of mechanical properties as lines instead of points and as planes instead of curves. Within our study here, we tried to consider this issue by testing more than 50 Charpy impact test samples and by confirming some of the BDT temperatures by additional tests. However, we did no statistics in the sense of determining a Weibull distribution, as is common practice for ceramics.

Nevertheless, we assume that our results show some interesting findings and that our results can act as a starting point and motivation for more systematic tests.

6. Conclusion

The identification of the controlling mechanisms of the BDT is a scientific challenge spanning many different length scales. At the upper end, it is the macroscopic dimension of the samples that causes the macroscopic stress distribution. At the lower end of the length scale, it is the breaking of individual atomic bonds. In between, there is the microstructure, providing dislocation sources, obstacles, and preferred crack paths.

Coming back to the main questions from chapter 1, we can conclude:

(1) For samples in the L-S and T-S orientations, the BDT decreases with cold-rolling.

(2) The BDT temperature correlates with the grain size in the S-direction. The anisotropy of the BDT temperature is related to the anisotropic grain shape.

(3) The shift of the BDT is primarily a dislocations effect. In the ductile regime we observed no microcracking, no branching of the main crack and no crack bridging.

In the Discussion section, the questions of what mechanisms increase the cleavage resistance stress, σ_F, and how cold-rolling increases the cleavage resistance stress, σ_F, are addressed. The main results can be summarized as follows:

- **Microcracking, crack branching, and crack bridging effects:** have not been observed in the ductile regime.
- **Crystallographic texture:** we do not think that texture effects are the most important parameter responsible for the decrease of the BDT temperature.
- **Impurities, micropores, and sinter pores:** grain boundaries are expected to be the weakest link in the chain. However, the "hot-rolled" and "cold-rolled" materials showed primarily transgranular fracture. So we do not think that impurities effects are the most important parameter responsible for the decrease of the BDT temperature.
- **Role of dislocations:** from our results it can be derived that the BDT correlates with grain size. Based on the Hall-Petch relationship, a constitutive equation between the BDT temperature and the mean grain size can be established. This equation might have a predictive power and should now be verified by systematic tests. Our results suggest that the availability of dislocation sources is responsible for the shift of the BDT to lower temperatures. These sources might be dislocation boundaries (segments of dislocation networks forming low-angle boundaries act as Frank-Read or Bardeen-Herring sources) and grain boundaries (boundary ledges that provide sites for dislocation nucleation). This underlines the importance of an in-depth understanding of the role of dislocations and addresses the question of how boundary source theories can contribute to a profound understanding of the shift of the BDT to lower temperatures through cold-rolling.

Our results will advance or have an impact on several research fields:
- From the technical point of view, tungsten materials with an improved BDT temperature might be interesting for the European Spallation Source (ESS), nuclear fusion applications, concentrated solar power applications, waste incineration or the production of biomass-to-liquid fuels (BTL fuels, pyrolysis [67]).
  At the ESS, tungsten has been chosen as the target material [68]. During the production of spallation neutrons, the tungsten target is subjected to fluctuating thermal loads with a maximum temperature of 500°C. Thus, a tungsten material with advanced mechanical properties is required [69].
  For nuclear fusion applications, tungsten is an interesting candidate both for the plasma-facing armour material [70,71] and for the structural cooling pipe [45]. For both fields of application, a tungsten material with an enhanced toughness is desirable.
  Concentrated solar power (CSP) systems and in particular next-generation central receiver systems will require higher operating temperatures and larger heat-flux densities. Advanced heat transfer fluids that can address these challenges are liquid metals [72]. The combination of high operation temperatures and liquid metal fluids makes tungsten an interesting candidate [73] (e.g. the alkali-metal thermal to electric converter, AMTEC [74]).
- From the scientific perspective, it should be noted that our results are in line with a series of recent publications showing the positive influence of cold-rolling on ductility [43], toughness [44,45] and the BDT [29] in tungsten. Németh et al. evaluated the nature of the BDT of annealed coarse-grained and as-received ultrafine-grained

(UFG) tungsten foil [29]. For the UFG tungsten foil they determined a BDT temperature of about 77 K, assuming that the BDT in UFG tungsten is controlled by the glide of edge dislocations. The work of Németh et al. leaves the question open whether the BDT temperature decreases continuously through cold-rolling, or if a decrease of the BDT temperature requires a UFG microstructure. From the results of our study presented in this paper, it can be derived that the shift of the BDT temperature is a continuous process and that also for coarse-grained tungsten the BDT can be shift to lower temperatures through cold-rolling (at least for the L-S and T-S directions). Now the question arises of how the tungsten microstructure changes during cold-rolling (e.g. subdivision of grains by deformation-induced boundaries such as GNBs and IDBs, formation of LAGBs and HAGBs [75,76]) and how such changes affect the cleavage resistance stress, σ_F, and thus the BDT temperature.

A number of mechanisms have been proposed to explain the shift of the BDT temperature through cold-rolling, or in other words to explain the increase of the cleavage resistance stress through cold-rolling: (i) a large amount of edge dislocations, (ii) the density of mixed, edge and screw dislocations, (iii) the number of active dislocation sources, (iv) boundaries acting as dislocation sources, and more. However, significantly more experiments and systematic studies are needed to elucidate the role of dislocations on the shift of the BDT through cold-rolling. Such an in-depth understanding might also advance research on the nature of the BDT of polycrystalline bcc materials and might even advance the research on the mechanisms controlling the classic Hall-Petch relation for strength.

Acknowledgements

References

[1]   Schmid E. in: Proc Internat Congr Appl Mech, Delft 1924:342.
[2]   Seeger A, Wasserbäch W. Phys Status Solidi A 2002;189:27.
[3]   Seeger A. Mat Sci Eng A-Struct 2001;319:254.
[4]   Seśták B, Seeger A. Z Metallkd 1978;69:195.
[5]   Christian JW. Metall Trans A 1983;14A:1237.
[6]   Hirsch PB. In: Proc. Fifth Internat. Conf. Crystallography, Cambridge, 1960 (Cambridge Press, Cambridge, 1960).
[7]   Vitek V, Perrin RJ, Bowen DK. Philos Mag 1970;21:1049.
[8]   Hull D, Bacon DJ. Introduction to Dislocations, fifth edition, Elsevier Ltd. 2011.
[9]   Gumbsch P. J Nucl Mater 2003;323:304.
[10]   Rice JR, Thomson R. Philos Mag 1974;29:73.
[11]   Khantha M, Pope DP, Vitek V. Phys Rev Lett 1994;74:684.
[12]   Hirsch PB, Roberts SG, Samuels J. P Roy Soc Lond A Mat 1989;421:25.
[13]   Roberts SG, in: Kirchner HO, Kubin LP, Pontikis V (Eds.), Computer Simulations in Materials Science, series E: Applied Sciences 1996;308:409.
[14]   Gumbsch P, Riedle J, Hartmaier A, Fischmeister HF. Science 1998;282:1293.
[15]   Giannattasio A, Tanaka M, Joseph TD, Roberts, SG. Phys Scripta 2007;T128:87.
[16]   Giannattasio A, Roberts, SG. Philos Mag 2007;87:2590.
[17]   Ohr SM. Mater Sci Eng 1985;72:1.

[18] Higashida K, Narita N, Onodera R, et al. Mat Sci Eng A-Struct 1997;237:72.
[19] Tanaka M, Higashida K, Kaneko K, et al. Scripta Mater 2008;59:901.
[20] Samuels J, Roberts SG. P Roy Soc Lond A Mat 1989;421:1.
[21] Schadler HW. Acta Metall Mater 1964;12:861.
[22] Seeger, A. Z. Metallkd. 2002;93:760.
[23] Brunner D. Mater T JIM 2000;41:152.
[24] Giannattasio A, Yao Z, Tarleton E, Roberts SG. Philos Mag 2010;90:3947.
[25] Rupp D, Weygand SM. Philos Mag 2010;90:4055.
[26] Rupp D. Bruch und Spröd-duktil-Übergang in polykristallinem Wolfram: Einfluss von Mikrostruktur und Lastrate, Dissertation, Karlsruhe Institute of Technology, 2010.
[27] Zeng XH, Hartmaier A. Acta Mater 2010;58:301.
[28] Hartmaier, A. Private communication, 2014.
[29] Németh AAN, Reiser J, Armstrong DEJ, Rieth M. Int J Refract Met H 2015;50:9.
[30] www.plansee.com, 2013.
[31] Annual Book of ASTM Standards—Standard Test Method for Plane-Strain Fracture Toughness of Metallic Materials (ASTM E 399–90), vol. 03.01, American Society for Testing and Materials 1997.
[32] Rieth M, Hoffmann A. Int J Refract Met H 2010;28:679.
[33] Veleva L, Schäublin R, Ramar A, et al. Focused Ion Beam application on the investigation of tungsten-based materials for fusion application, Proceedings, Springer, Berlin, 2008.
[34] Lassner E, Schubert WD. Tungsten - Properties, Chemistry, Technology of the Element, Alloys, and Chemical Compounds, Springer, Berlin, 1999.
[35] Pantleon W. Mat Sci Eng A-Struct 2005;400:118.
[36] Mrotzek T, Hoffmann A, Martin U. Work Hardening of the Molybdenum Alloy TZM, PLANSEE seminar 2009.
[37] Hall EO. Proc Phys Soc 1951;B 64:747.
[38] Petch NJ. I Iron Steel Inst 1953;174:25.
[39] Li JCM, Chou YT. Met Trans 1970;1:1145.
[40] Gladman T, Pickering FB. The effect of grain size on the mechanical properties of ferrous materials. In: Baker TN, editor. Yield, flow and fracture of polycrystals. London: Applied Science Publishers; 1983:148.
[41] Morris Jr JW, Lee CS, Guo Z. ISIJ Int 2003;3:410.
[42] Inoue T, Yin F, Kimura Y, et al. Metall Mater Trans A 2010;41A:341.
[43] Wei Q, Kecskes LJ. Mat Sci Eng A-Struct 2008;491:62.
[44] Pippan R, presented at W conference, organized by Odette GR, UCLA, Santa Barbara, USA, February 2011.
[45] Reiser J, Rieth M, Möslang A, et al. Adv Eng Mater 2015;17:491.
[46] Fünfschilling S, Fett T, Hoffmann MJ, et al. Acta Mater 2011;59:3978.
[47] Oertel CG, Hüsche I, Skrotzki W, et al. Int J Refract Met H 2010;28:722.
[48] Neges J, Ortner B, Leichtfried, Stüwe HP. Mat Sci Eng A-Struct 1995;196:129
[49] Gludovatz B, Wurster S, Hoffmann A, Pippan R. Int J Refract Met H 2010;28:674.
[50] Tran-Huu-Loi, Morniroli JP, Gantois M, Lahaye M. J Mater Sci 1985;20:199.
[51] Funkenbusch AW, Bacon F, Lee D. Metall Trans A 1979;10:1085.
[52] Joshi A, Stein DF. Metall Trans 1970;1:2543.
[53] Danninger H, Knoll F, Lux B, Wilhartitz P, Grasserbauer M. Int J Refract Met H 1985;4:92.
[54] Gludovatz B, Wurster S, Weingartner T, Hoffmann A, Pippan R. Philos Mag 2011;91:1.
[55] Hoffmann A, Wesemann I. Int J Powder Metall 2011;47:1.
[56] Cheng GM, Jian WW, Xu WZ, Yuan H, Millett PC, Zhu YT. Mater Res Lett 2013;1:26.
[57] Reiser J, Rieth M, Möslang A, Dafferner B, Hoffmann A, Yi X, Armstrong DEJ. J Nucl Mater 2013;434:357.
[58] Pickering FB. Physical metallurgy and the design of steels. London: Applied Science Publishers; 1978:16.
[59] Song R, Ponge D, Raabe D. Acta Mater 2005;53:4881.

[60]   Cracknell A, Ptech NJ. Acta Met 1955;3:186.
[61]   Plickering FB, Gladman T. ISI Spec Rep No 81, 1963, Iron and Steel Institute, London, p. 10.
[62]   Hohenwarter A, Pippan R. Acta Mater. 2013;61:2973.
[63]   Gizynski M, Pakiela Z, Chrominski W, Kulczyk M. Mat Sci Eng A-Struct 2015;632:35.
[64]   Reiser J, Rieth M, Dafferner B, Hoffmann A. J Nucl Mater 2013;442:S204.
[65]   Eck R, Pink E. Int J Refract Met H 1992;11:337.
[66]   Northcott L. J Less-Common Met 1961;3:125.
[67]   Dahmen N, Dinjus E, Kolb T, Arnold U, Leibold H, Stahl R. Environ Prog 2012;31:176.
[68] S. Peggs, in: ESS Conceptual Design Report, Feb 6, 2012, ISBN: 978-91-980173-0-4.
[69]   Pasalic M, Rustempasic F, Iyengar S, et al. Int J Refract Met H 2014;42:163.
[70]   Zhang X, Yan Q. J Nucl Mater 2014;444:428.
[71]   Hirai T, Pintsuk G, Linke J, Batilliot. J Nucl Mater 2009;390:751.
[72]   Pacio J, Singer Cs, Wetzel Th, Uhlig R. Appl Therm Eng 2013;60:295.
[73]   Wu S-Y, Xiao L, Cao Y, Li, Y-R. Appl Energ 2010;87:452.
[74]   Hering W, Stieglitz R, Wetzel T. Application of liquid metals for solar energy systems, EPJ Web of Conferences 33 (2012) 03003.
[75]   Hansen N. Metall Mater Trans A 2001;32A:2917.
[76]   Hughes DA, Hansen N. Acta Mater 1997;45:3871.